Geophysical Journal International

Geophys. J. Int. (2018) **215,** 1540–1557
Advance Access publication 2018 August 23
GJI Gravity, geodesy and tides

doi: 10.1093/gji/ggy351

Joint multinary inversion of gravity and magnetic data using Gramian constraints

Wei Lin[1,2] and Michael S. Zhdanov[1,3]

[1]*Department of Geology and Geophysics, University of Utah, Salt Lake City, UT* 84112*, USA. E-mail: u0703769@utah.edu*
[2]*Minmetals Exploration and Development Company, Beijing* 100010*, China*
[3]*TechnoImaging, Salt Lake City, UT* 84107*, USA*

Accepted 2018 August 21. Received 2018 August 7; in original form 2018 May 20

SUMMARY

This paper proposes a novel approach to the joint inversion of gravity and magnetic data based on multinary transformation of the model parameters and Gramian constraints. The concept of multinary transformation is a generalization of the binary density inversion for models described by any number of discrete model parameters, while the Gramian constraint enforces the linear relationships between the different model parameters and their attributes or transforms. By combining these two concepts, the joint multinary inversion using Gramian constraints not only makes it possible to explicitly exploit the sharp contrasts of the density and magnetic susceptibility between the host media and anomalous targets in the inversion of gravity and magnetic data, but also provides uniform spatial boundaries of the anomalous targets in the distributions of density and magnetic susceptibility. The novel joint multinary inversion algorithm is demonstrated to be effective in determining the shapes, locations and physical properties of the anomalous targets. We show that this method can be effectively applied to the joint inversion of the full tensor gravity gradiometry data and the total magnetic intensity data, computer simulated for 3-D synthetic models using ternary model transformation. We also tested this joint inversion algorithm in the area of the McFaulds Lake in northwestern Ontario, Canada, and the joint inversion results provide a reasonable geological model with high resolution for the exploration of magmatic chromite deposits.

Key words: Joint inversion, Inverse theory.

1 INTRODUCTION

It is well known that the inversion of potential field data is a non-unique problem. One approach to reduce the non-uniqueness is based on the joint inversion of the multimodal data (e.g. gravity and magnetic), if the corresponding physical properties (e.g. density and magnetic susceptibility) are mutually correlated. Over the years, different techniques have been developed for joint inversion algorithms. For example, if the direct functional relationships between the different physical properties are known *a priori*, then one can apply a method based on the direct joint parameter inversion (e.g. Vozoff & Jupp 1975). In a case where different physical properties can be expressed by different functionals of the same intrinsic petrophysical properties (e.g. porosity, water saturation), one can invert the different observed geophysical data jointly for these intrinsic properties (e.g. Abubakar *et al.* 2012; Gao *et al.* 2012). The cross-gradient constraint is a popular solution for the joint inverse problem when the different physical properties are not correlated but have similar geometrical structures. The cross-gradient constraint enforces the structural similarities between the different physical properties by minimizing the parametric functional with the cross-gradient term (Haber & Oldenburg 1997; Gallardo & Meju 2003, 2004, 2011; Colombo & De Stefano 2007).

Zhdanov *et al.* (2012) introduced a unified approach to the joint inversion of different geophysical data using Gramian constraints. By imposing an additional requirement of minimizing the Gramian during the regularized inversion, one can recover multiple model parameters with enhanced correlation between the different physical properties and/or their attributes (Lin & Zhdanov 2017).

Another complication of geophysical inversion is that the traditional inversions of potential field data usually characterize the distributions of physical properties by a function, which varies continuously within the given bounds (Zhdanov 2002, 2015). In order to improve the resolution of the inversions of potential field data, several techniques have been developed which aid the recovery of anomalous targets with high contrasts between physical properties and sharp boundaries. For example, one can use focusing regularization (Portniaguine & Zhdanov 1999; Zhdanov 2002, 2015) to recover model parameters with sharp physical property contrasts. However, all these methods still produce a continuous distribution

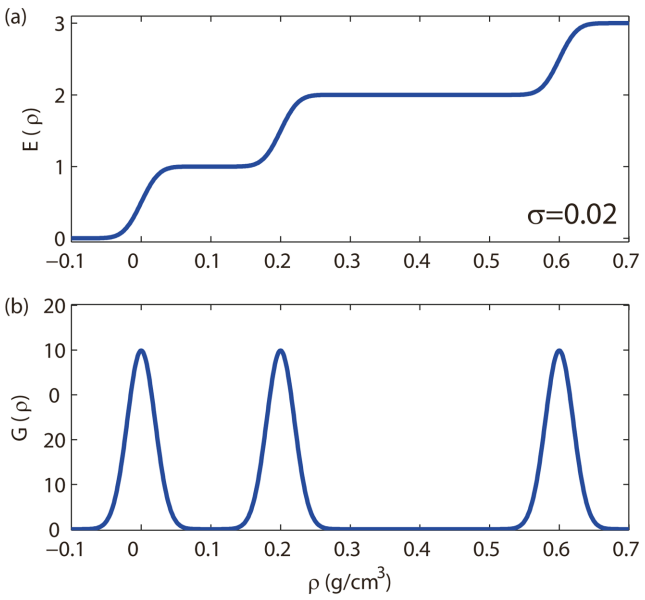

Figure 1. An example of the multinary model transform: (a) multinary function of the third order, $E(\rho)$, (b) its derivative, $G(\rho)$. The values of the discrete densities are as follows: 0, 0.2 and 0.6 g cm^{-3}, and $\sigma = 0.02$.

of the physical properties, even if the inverse images become more focused and sharp.

In the papers by Zhdanov & Cox (2013) and Zhdanov & Lin (2017), the multinary inversion algorithm was proposed to explicitly exploit the sharp contrasts of the density between the host media and anomalous targets in the inversion of gravity data. This method is a generalization of binary density inversion for models described by any number of discrete model parameters (e.g. Bosch *et al.* 2001; Krahenbuhl & Li 2006) or of a level set method (e.g. Osher & Sethian 1988; Santosa 1996; Dorn & Lesselier 2006).

In the mineral exploration, one would expect the recovered boundaries of ore body derived from different geophysical data sets to be consistent, as they represent the same geological structure. Recently Zheglova & Farquharson (2018) proposed a multiple level-set algorithm for joint inversion of traveltime and gravity data. By combining the seismic and gravity data, the resolution of the results of joint inversion was improved compared to separate inversions. However, due to the known limitations of the level-set method, each local field anomaly should correspond to one initial convex anomalous model, which may require using some *a priori* information for the joint inversion (e.g. spatial locations, physical properties, approximate sizes, etc.), which is not always available. To this end, we propose a novel approach to the joint inversion of gravity and magnetic data based on multinary transformation of the model parameters and Gramian constraints. By combining these two concepts, the joint multinary inversion using Gramian constraints makes it possible not only to provide sharp contrasts of the density and magnetic susceptibility between the host media and anomalous targets in the inverse models, but also to recover the same spatial boundaries of the anomalous targets in the distributions of density and magnetic susceptibility.

We have developed an algorithm for the joint multinary inversion for gravity and magnetic data using Gramian constraints. The method was tested on 3-D synthetic models with different combinations of densities and magnetic susceptibilities using ternary model transformation. We have also tested this algorithm in the joint inversion of gravity and magnetic data in the area of McFaulds Lake of northwestern Ontario of Canada.

2 POTENTIAL FIELD FORWARD MODELLING

The forward modelling of gravity and magnetic responses can be expressed by linear operators with respect to density ρ and magnetic susceptibility χ, as follows:

$$\mathbf{d}^{\mathrm{g}} = \mathbf{A}^{\mathrm{g}}(\rho),\ \mathbf{d}^{\mathrm{m}} = \mathbf{A}^{\mathrm{m}}(\chi), \tag{1}$$

where $\mathbf{A}^{\mathrm{g}}$ and $\mathbf{A}^{\mathrm{m}}$ are the linear forward modelling operators for gravity and magnetic fields, respectively.

2.1 Gravity forward modelling

The gravity field can be computed as the gradient of the gravity potential U:

$$\mathbf{g}(\mathbf{r}) = \nabla U(\mathbf{r}) = \gamma \iiint_D \rho(\mathbf{r}') \frac{\mathbf{r}' - \mathbf{r}}{|\mathbf{r}' - \mathbf{r}|^3} \mathrm{d}v, \tag{2}$$

where the gravity potential, U, has the following form:

$$U(\mathbf{r}) = \gamma \iiint_D \frac{\rho(\mathbf{r}')}{|\mathbf{r}' - \mathbf{r}|} \mathrm{d}v. \tag{3}$$

The second spatial derivatives of the gravity potential U can be expressed as follows:

$$g_{\alpha\beta}(\mathbf{r}) = \frac{\partial^2}{\partial\alpha\partial\beta} U(\mathbf{r}), \alpha, \beta = x, y, z. \tag{4}$$

They form a symmetric gravity tensor

$$\widehat{\mathbf{g}} = \begin{bmatrix} g_{xx} & g_{xy} & g_{xz} \\ g_{yx} & g_{yy} & g_{yz} \\ g_{zx} & g_{zy} & g_{zz} \end{bmatrix}. \tag{5}$$

The expressions for the gravity tensor components can be written as follows:

$$g_{\alpha\beta}(\mathbf{r}) = \gamma \iiint_D \frac{\rho(\mathbf{r}')}{|\mathbf{r}' - \mathbf{r}|^3} K_{\alpha\beta}(\mathbf{r}' - \mathbf{r}) \mathrm{d}v, \tag{6}$$

where kernels $K_{\alpha\beta}$ are equal to

$$K_{\alpha\beta}(\mathbf{r}' - \mathbf{r}) = \begin{cases} \frac{3(\alpha - \alpha')(\beta - \beta')}{|\mathbf{r}' - \mathbf{r}|^2}, \alpha \neq \beta \\ \frac{3(\alpha - \alpha')^2}{|\mathbf{r}' - \mathbf{r}|^2} - 1, \alpha = \beta \end{cases}, \alpha, \beta = x, y, z. \tag{7}$$

2.2 Magnetic forward modelling

Generally, it is assumed that the self-demagnetization effects can be negligible and the magnetic susceptibility is isotropic, so that there would be no remanent magnetization. Under this assumption, the intensity of magnetization, $\mathbf{I}(\mathbf{r})$, is linearly related to the inducing magnetic field, $\mathbf{H}_0(\mathbf{r})$,

$$\mathbf{I}(\mathbf{r}) = \chi(\mathbf{r})\mathbf{H}_0(\mathbf{r}) = \chi(\mathbf{r})H_0\mathbf{l}(\mathbf{r}), \tag{8}$$

where $\chi(\mathbf{r})$ is the magnetic susceptibility and $\mathbf{l}(\mathbf{r}) = (l_x, l_y, l_z)$ is the unit vector along the direction of the inducing field. Assuming that the x-axis is directed eastwards, the y-axis has a positive direction northwards, and the z-axis is downwards, the direction of the

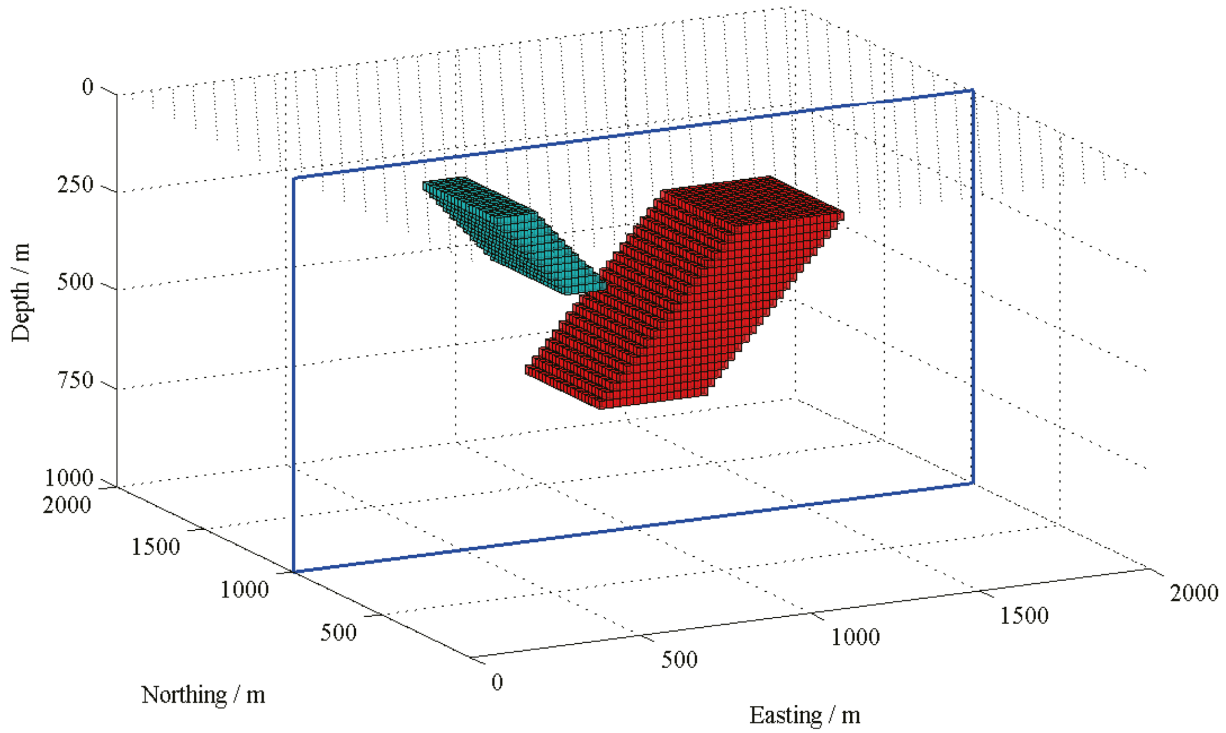

Figure 2. Model study 1. A 3-D view of the synthetic model. The rectangular contour outlines the location of the cross-section shown in the next figures. The black dots show the locations of the receivers of the gravity and magnetic data.

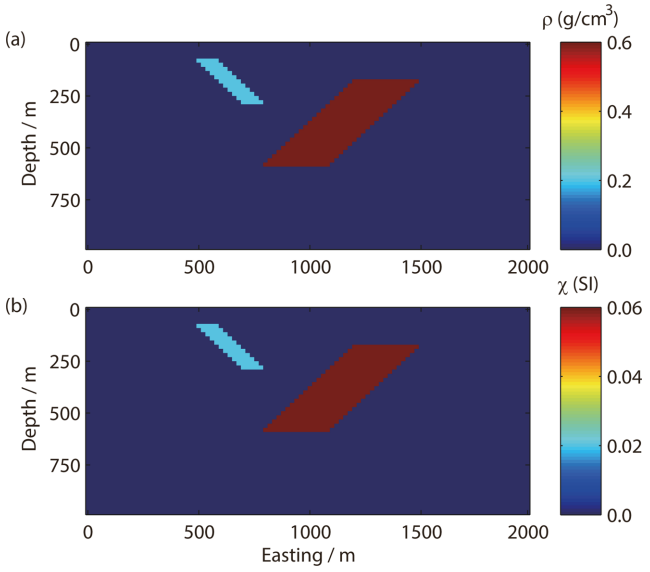

Figure 3. Model study 1. Panel (a) shows a cross-section of the synthetic density distribution of the model; panel (b) presents a cross-section of the synthetic magnetic susceptibility distribution.

inducing magnetic field can be computed as follows:

$$\begin{aligned} l_x &= \cos(I)\sin(D-A), \\ l_y &= \cos(I)\cos(D-A), \\ l_z &= \sin(I), \end{aligned} \tag{9}$$

for given inclination (I), declination (D) and azimuth (A) from the International Geomagnetic Reference Field.

Thus, the anomalous magnetic field can be represented in the following form:

$$\mathbf{H}(\mathbf{r}) = -\frac{H_0}{4\pi}\iiint_D \frac{\chi(\mathbf{r}')}{|\mathbf{r}'-\mathbf{r}|^3}\left[\mathbf{l}-\frac{3(\mathbf{l}\cdot(\mathbf{r}'-\mathbf{r}))(\mathbf{r}'-\mathbf{r})}{|\mathbf{r}'-\mathbf{r}|^2}\right]\mathrm{d}v. \tag{10}$$

In the airborne magnetic survey, the total magnetic intensity (TMI) field is measured, which can be computed approximately as follows:

$$T(\mathbf{r}) \approx \mathbf{l}\cdot\mathbf{H}(\mathbf{r}) = -\frac{H_0}{4\pi}\iiint_D \frac{\chi(\mathbf{r}')}{|\mathbf{r}'-\mathbf{r}|^3}\left[1-\frac{3(\mathbf{l}\cdot(\mathbf{r}'-\mathbf{r}))^2}{|\mathbf{r}'-\mathbf{r}|^2}\right]\mathrm{d}v. \tag{11}$$

One can use the point-mass approximation to calculate formulae (7) and (11) in the discrete form by considering each cell as a point mass (Zhdanov 2009).

3 JOINT INVERSION USING GRAMIAN CONSTRAINTS

In this section, we will summarize the theory of joint inversion using Gramian constraints. One can find more details about this method in Zhdanov *et al.* (2012), Zhdanov (2015), Zhu (2017) and Lin & Zhdanov (2017).

Consider two different geophysical data sets, $\mathbf{d}^{(j)}$ $(j = 1, 2)$, representing gravity and magnetic data, respectively, and the related two physical properties, $\mathbf{m}^{(j)}$ $(j = 1, 2)$, \$ representing density (ρ) and magnetic susceptibility (χ), respectively. The joint inversion for these two model parameters can be formulated as a minimization of a single parametric functional according to the following formula

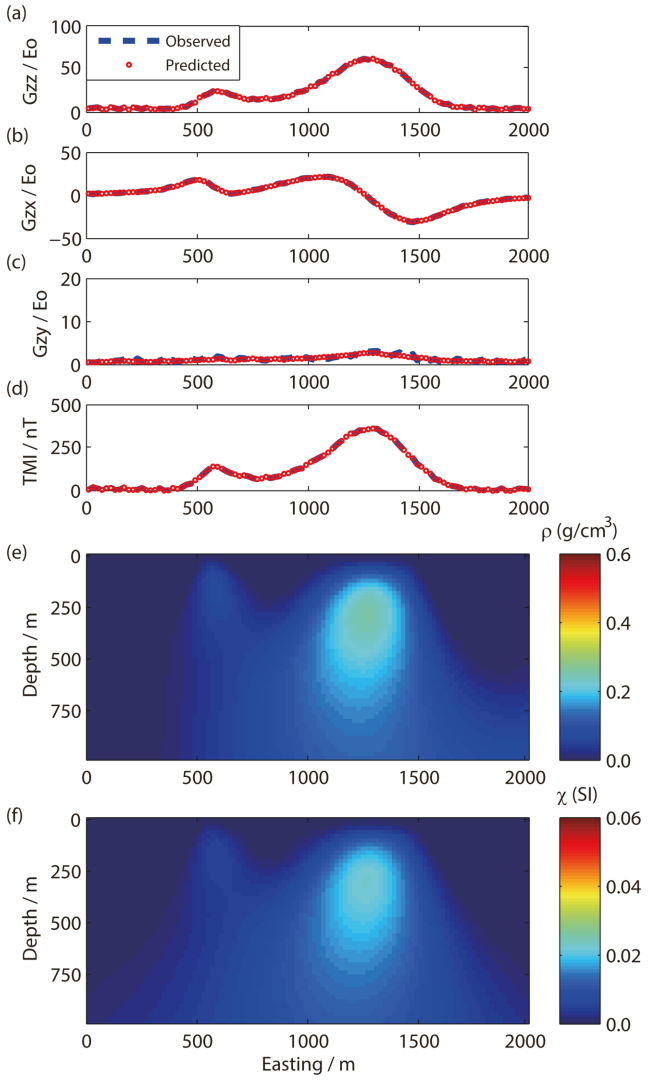

Figure 4. Case 1 of model study 1: separate minimum norm inversions. Synthetic data (dashed line) versus predicted data (dotted line) along the cross-section in Fig. 2 for the FTG components, (a) G_{zz}, (b) G_{zx}, (c) G_{zy} and (d) TMI data. Panel (e) shows the cross-section of the recovered density distribution; panel (f) shows the cross-section of the inverse magnetic susceptibility model.

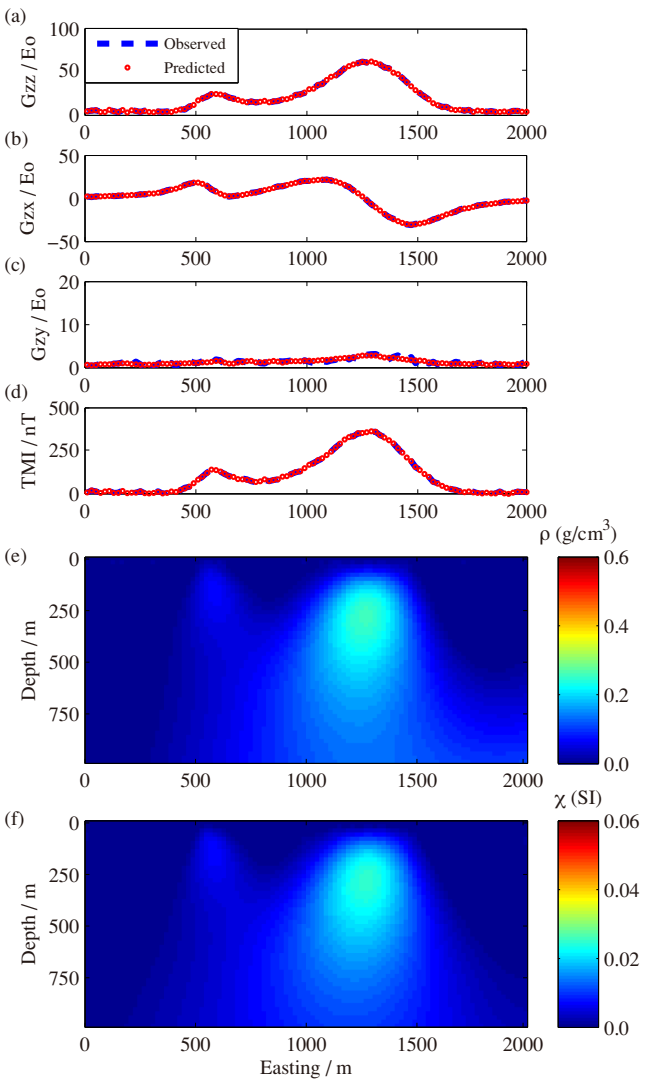

Figure 5. Case 2 of model study 1: joint minimum norm inversion with structural Gramian constraint. Synthetic data (dashed line) versus predicted data (dotted line) along the cross-section in Fig. 2 for the FTG components, (a) G_{zz}, (b) G_{zx}, (c) G_{zy} and (d) TMI data. Panel (e) shows the cross-section of the recovered density distribution; panel (f) shows the cross-section of the inverse magnetic susceptibility model.

(Zhdanov *et al.* 2012; Zhdanov 2015):

$$P^{\alpha}(\mathbf{m}^{(1)}, \mathbf{m}^{(2)}) = \sum_{j=1}^{2} \varphi_{\mathrm{w}}^{(j)}(\mathbf{m}^{(j)}) + \sum_{j=1}^{2} \alpha^{(j)} s_{\mathrm{MN}}(\mathbf{m}^{(j)}) + \beta S_{\mathrm{G}}(L\mathbf{m}^{(1)}, L\mathbf{m}^{(2)}), \tag{12}$$

where $\varphi_{\mathrm{w}}^{(j)}(\mathbf{m}^{(j)})$ are the misfit functionals of the weighted data:

$$\varphi_{\mathrm{w}}^{(j)}(\mathbf{m}^{(j)}) = \left\| \mathbf{W}_{\mathrm{d}}^{(j)}(\mathbf{A}^{(j)}(\mathbf{m}^{(j)}) - \mathbf{d}^{(j)}) \right\|_{L_2}^2, \quad j = 1, 2, \tag{13}$$

and the data weighting matrix, $\mathbf{W}_{\mathrm{d}}^{(j)}$, is selected as the inverse norm of each geophysical data set, $\|\mathbf{d}^{(j)}\|_{L_2}^{-1}$.

In formula (12), the coefficients $\alpha^{(j)}$ and β are chosen as follows:

$$\alpha^{(j)} = \frac{\varphi_{\mathrm{w}}^{(j)}(\mathbf{m}^{(j)})}{s_{\mathrm{MN}}(\mathbf{m}^{(j)})}, \quad j = 1, \ 2; \tag{14}$$

$$\beta = \frac{\sum_{j=1}^{2} \varphi_{\mathrm{w}}^{(j)}(\mathbf{m}^{(j)})}{S_{\mathrm{G}}(L\mathbf{m}^{(1)}, L\mathbf{m}^{(2)})}. \tag{15}$$

The minimum norm stabilizing functionals in the weighted model space, $S_{\mathrm{MN}}^{(j)}$, are calculated as follows:

$$S_{\mathrm{MN}}^{(j)} = \left\| \mathbf{W}_{\mathrm{m}}^{(j)}(m^{(j)} - m_{\mathrm{apr}}^{(j)}) \right\|_{L_2}^2, \quad j = 1, 2. \tag{16}$$

Note that, the model weighting matrix, $\mathbf{W}_{\mathrm{m}}^{(j)}$, is defined as a square root of the integrated sensitivity matrix, which can be treated as a depth weighting factor in the inversion algorithm (Zhdanov 2002).

It is known that the joint inversion of different geophysical data sets may be unstable due to the fact that different physical properties have different units and magnitudes. In order to eliminate these negative factors, we work with the normalized dimensionless data and model parameters.

In the formula (12), the coefficients $\alpha^{(j)}$ and β are some positive numbers introduced for weighting the different parts of the

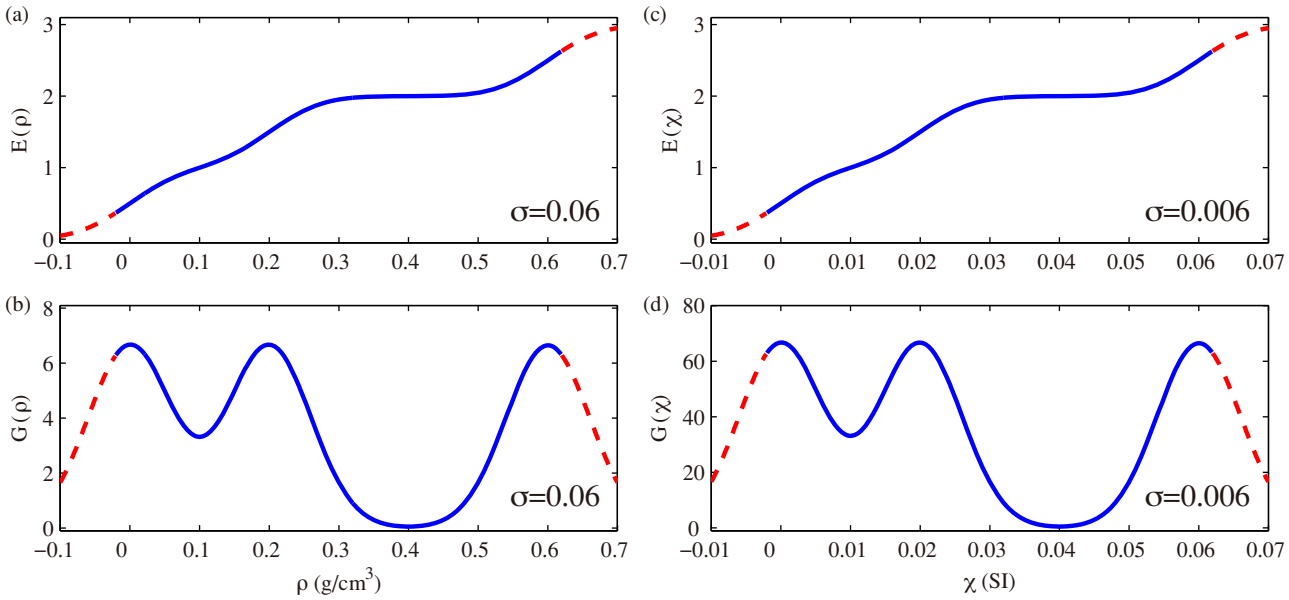

Figure 6. Case 3 of model study 1: separate multinary inversions. Panels (a) and (c) show the approximate representations of the ternary model transforms for density (ρ) and magnetic susceptibility (χ), respectively, and panels (b) and (d) show their derivatives. The values of the discrete densities and magnetic susceptibilities are as follows: 0, 0.2 and 0.6 g cm^{-3}, and $\sigma^{(1)} = 0.06$; 0, 0.02 and 0.06 SI, and $\sigma^{(2)} = 0.006$. The dashed lines in these plots correspond to the values of density and magnetic susceptibility outside of the upper and lower bounds imposed in the inversion.

parametric functional. The term $S_{\rm G}(L\mathbf{m}^{(1)}, L\mathbf{m}^{(2)})$is the Gramian constraint (Zhdanov *et al.* 2012), which in a case of two physical properties can be written, using matrix notations, as follows:

$$S_{\rm G}(L\mathbf{m}^{(1)}, L\mathbf{m}^{(2)}) = \begin{vmatrix} (L\mathbf{m}^{(1)}, L\mathbf{m}^{(1)}) & (L\mathbf{m}^{(1)}, L\mathbf{m}^{(2)}) \\ (L\mathbf{m}^{(2)}, L\mathbf{m}^{(1)}) & (L\mathbf{m}^{(2)}, L\mathbf{m}^{(2)}) \end{vmatrix}, \tag{17}$$

where operator $L(j = 1, 2)$ represents some linear transformation of the model parameters, and operation $(\cdot, \cdot)$ stands for the inner product of two vectors in the corresponding Gramian space (Zhdanov, 2015). It is clear that the determinant, $S_{\rm G}(L\mathbf{m}^{(1)}, L\mathbf{m}^{(2)})$, approaches zero when the model parameters satisfy the following condition:

$$L\mathbf{m}^{(1)} = k \cdot L\mathbf{m}^{(2)}, \tag{18}$$

where k is some real number.

Thus, by minimizing the parametric functional (12), we enforce the linear correlation between the model parameters; however, different transforms of physical properties can be used as additional parameters as well. For example, if operator L is selected as the gradient operator, $L = \nabla$, then the Gramian requires that the gradients of the different model parameters will be parallel to each other, which is similar to the case of cross-gradient constraints (Zhdanov 2015). Note that, minimization of the Gramian of the gradients imposes the structural constraints which do not necessary require a direct correlation between the physical properties themselves. Therefore, the Gramian structural constraints can be used in the situation containing the rock formations with different types of relationships between density and susceptibility (e.g. igneous rocks with high density and magnetization, and carbonates with high density and no magnetization, $\chi = 0$).

4 MULTINARY MODEL TRANSFORM

Consider a gravity inverse problem with multinary model transform. It can be formulated as a solution of the following operator equation:

$$\mathbf{d}^{\rm g} = \mathbf{A}^{\rm g}(\rho), \tag{19}$$

where $\mathbf{A}^{\rm g}$ is a linear operator for computing the gravity field; $\mathbf{d}^{\rm g}$ are the observed gravity field data, which may include the gravity field, G_z, and all components of the full gravity gradient tensor and ρ represents the model density. In the case of a discrete inverse problem, the density distribution ρ can be represented as a vector formed by $N_{\rm m}$ components:

$$\rho = [\rho_1, \rho_2, ..., \rho_{N_{\rm m}}]^T, \tag{20}$$

and the observed data $\mathbf{d}$ can be considered as an $N_{\rm d}$ -dimensional vector,

$$\mathbf{d} = [d_1, d_2, ..., d_{N_{\rm d}}]^T, \tag{21}$$

where $N_{\rm m}$ is the number of unknown model parameters (e.g. the number of discretization cells in the inverse model); $N_{\rm d}$ is the number of data points; and superscript 'T' denotes the transposition operation.

The nonlinear transformation of the continuous function into the multinary function can be described as follows. The original vector of anomalous density distribution, $\rho = [\rho_1, \rho_2, ..., \rho_{N_{\rm m}}]^T$, is transformed into a new vector model space, $\widetilde{\rho} = [\widetilde{\rho}_1, \widetilde{\rho}_2, ..., \widetilde{\rho}_{N_{\rm m}}]^T$, defined by a number of discrete (multinary) densities, $\rho^{(j)}$ ($j = 1, 2, ...P$), using a superposition of error functions:

$$\widetilde{\rho}_i = E_\sigma(\rho_i) = c\rho_i + \frac{1}{2}\sum_{j=1}^{P}\left[1 + \mathtt{erf}\left(\frac{\rho_i - \rho^{(j)}}{\sqrt{2}\sigma}\right)\right], \; i = 1, ..., N_{\rm m}. \tag{22}$$

In the last formula, the error function, $\mathtt{erf}(z)$, $is defined as follows:

$$\mathtt{erf}(z) = \frac{2}{\sqrt{\pi}}\int_0^z e^{-t^2} dt, \tag{23}$$

where parameter σ is a standard deviation of the value $\rho^{(j)}$, constant c is a small number to avoid singularities in the calculation of the derivatives of the quasi-multinary densities, $\widetilde{\rho}_i$, and P is a total number of discrete (multinary) values of the model parameters

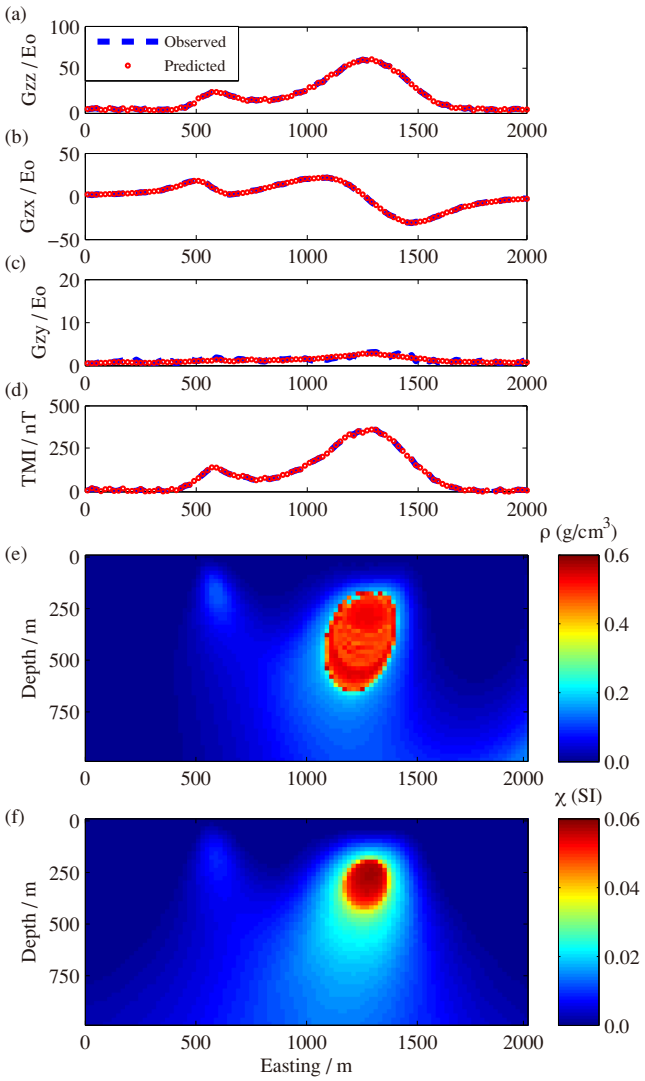

Figure 7. Case 3 of model study 1: separate multinary inversions. Synthetic data (dashed line) versus predicted data (dotted line) along the cross-section in Fig. 2 for the FTG components, (a) G_{zz}, (b) G_{zx}, (c) G_{zy} and (d) TMI data. Panel (e) shows the cross-section of the recovered density distribution; panel (f) shows the cross-section of the inverse magnetic susceptibility model.

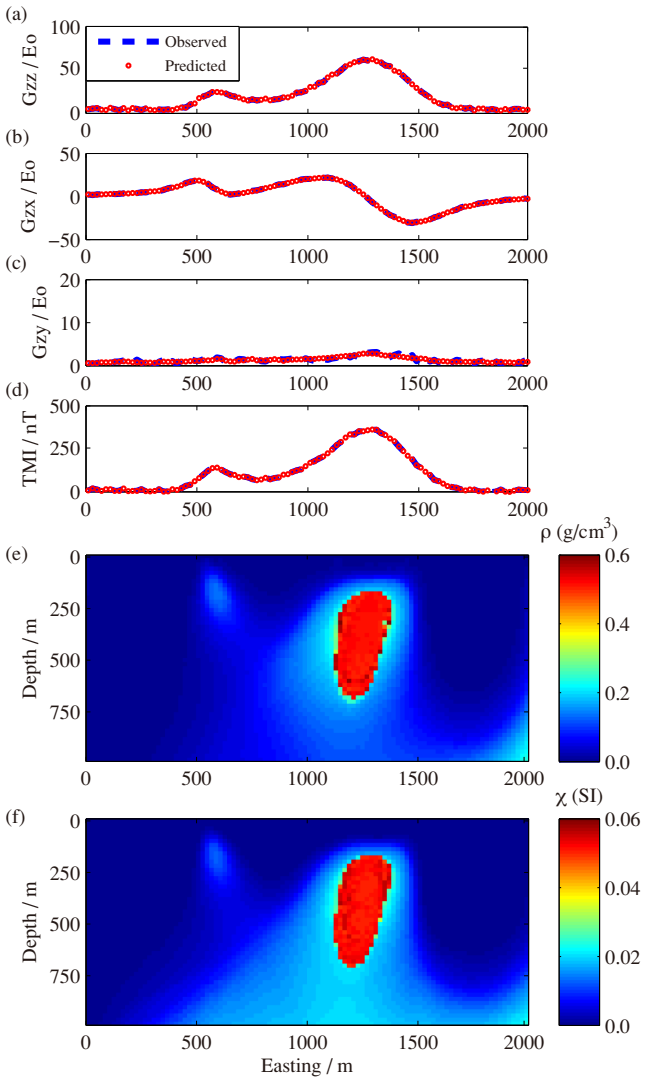

Figure 8. Case 4 of model study 1: joint multinary inversion with structural Gramian constraint. Synthetic data (dashed line) versus predicted data (dotted line) along the cross-section in Fig. 2 for the FTG components, (a) G_{zz}, (b) G_{zx} , (c) G_{zy} and (d) TMI data. Panel (e) shows the cross-section of the recovered density distribution; panel (f) shows the cross-section of the inverse magnetic susceptibility model.

(densities), $\rho^{(j)}$. The discrete densities, $\rho^{(j)}(j = 1, 2, ..., P)$, can be chosen *a priori* based on the known geological information (e.g. core samples).

Note that the derivative of the error function (22) is equal to the corresponding Gaussian function; therefore, the derivative of the quasi-multinary densities, $\widetilde{\rho}_i$, can be calculated as a superposition of the Gaussian functions, $G_\sigma\left(\rho_i - \rho_i^{(j)}\right)$, as follows:

$$\frac{\partial \widetilde{\rho}_i}{\partial \rho_i} = \frac{\partial E_\sigma(\rho_i)}{\partial \rho_i} = g_\sigma(\rho_i) = \sum_{j=1}^{P} G_\sigma\left(\rho_i - \rho_i^{(j)}\right) + c, \tag{24}$$

where

$$G_\sigma\left(\rho_i - \rho_i^{(j)}\right) = \frac{1}{\sqrt{2\pi}\sigma_i} \exp\left(\frac{-\left(\rho_i - \rho_i^{(j)}\right)^2}{2\sigma_i^2}\right). \tag{25}$$

Fig. 1(a) shows an example of the multinary model transform of three discrete densities, while Fig. 1(b) presents its derivative, where values of the discrete densities are as follows: 0, 0.2 and 0.6 g cm^{-3}, and $\sigma = 0.02$. One can see from this figure how a continuous distribution of the anomalous density along the horizontal axis can be transformed into the step-wise distribution, $E(\rho)$, along the vertical axis. It is important to note that the range of the parameters in the multinary model space depends on the order number of the multinary function. For example, the value of multinary model transform in Fig. 1 ranges from 0 to 3 for the case of ternary transformation with three discrete densities.

We can see from Fig. 1 that the multinary model transform (22) provides some flexibility of the transformed parameters which is required in practical applications in order to fit the observed data with the proper accuracy (Zhdanov & Lin 2017).

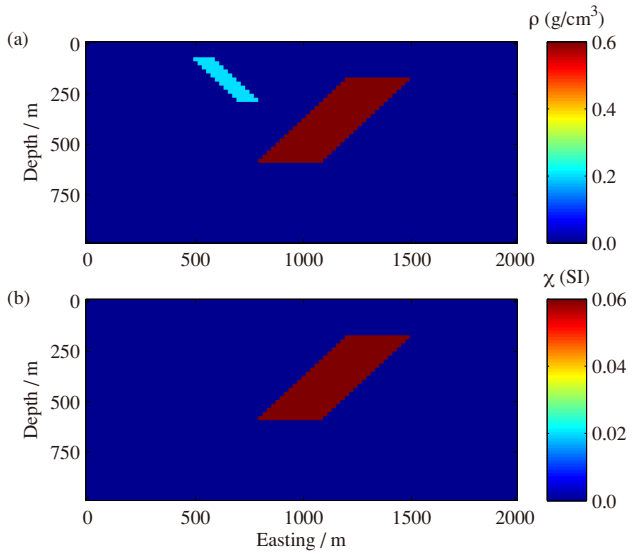

Figure 9. Model study 2. Panel (a) shows a cross-section of the synthetic density distribution of the model; panel (b) presents a cross-section of the synthetic magnetic susceptibility distribution.

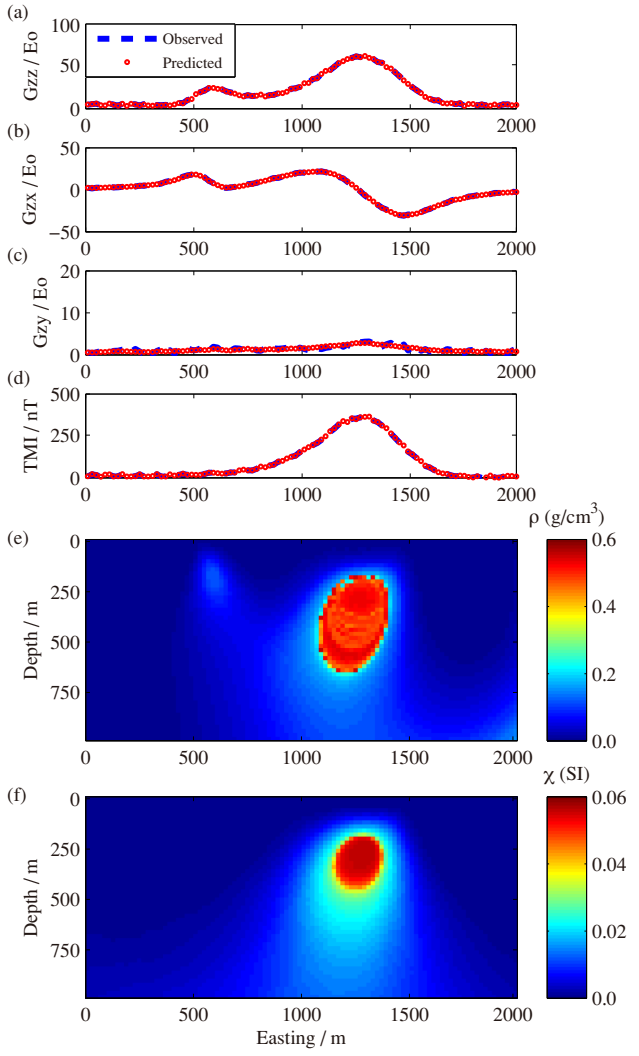

Figure 10. Case 1 of model study 2: separate multinary inversions. Synthetic data (dashed line) versus predicted data (dotted line) along the cross-section in Fig. 2 for the FTG components, (a) G_{zz}, (b) G_{zx}, (c) G_{zy} and (d) TMI data. Panel (e) shows the cross-section of the recovered density distribution; panel (f) shows the cross-section of the inverse magnetic susceptibility model.

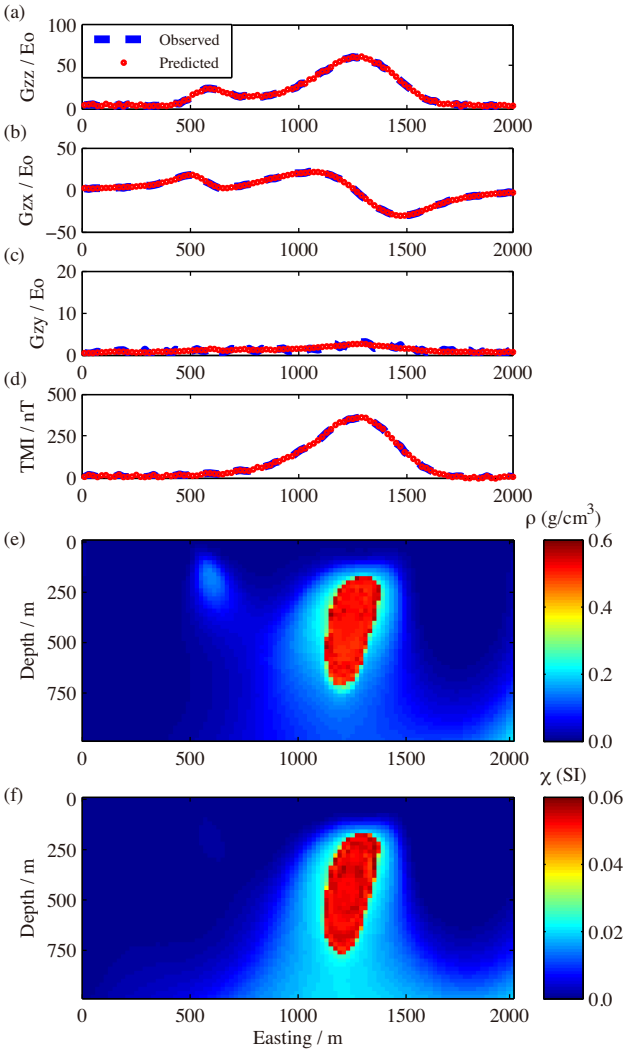

Figure 11. Case 2 of model study 2: joint multinary inversion with structural Gramian constraint. Synthetic data (dashed line) versus predicted data (dotted line) along the cross-section in Fig. 2 for the FTG components, (a) G_{zz}, (b) G_{zx} , (c) G_{zy} and (d) TMI data. Panel (e) shows the cross-section of the recovered density distribution; panel (f) shows the cross-section of the inverse magnetic susceptibility model.

5 JOINT MULTINARY INVERSION USING GRAMIAN CONSTRAINTS

In this section, we combine the above two concepts of Gramian constraints and multinary transform for the joint inversion of gravity and magnetic data.

First, we rewrite eq. (1) as follows:

$$\mathbf{d} = \mathbf{A}(\mathbf{m}). \tag{26}$$

In the last formula, we use the following notations: $\mathbf{d}$ is a vector of the observed gravity and magnetic data,

$$\mathbf{d} = \left[\mathbf{d}^{(1)},\ \mathbf{d}^{(2)}\right]^T = \left[\mathbf{d}^{\mathrm{g}},\ \mathbf{d}^{\mathrm{m}}\right]^T; \tag{27}$$

$\mathbf{m}$ is a vector of the model parameters (density and magnetic susceptibility),

$$\mathbf{m} = \left[\mathbf{m}^{(1)},\ \mathbf{m}^{(2)}\right]^T = [\rho,\ \chi]^T; \tag{28}$$

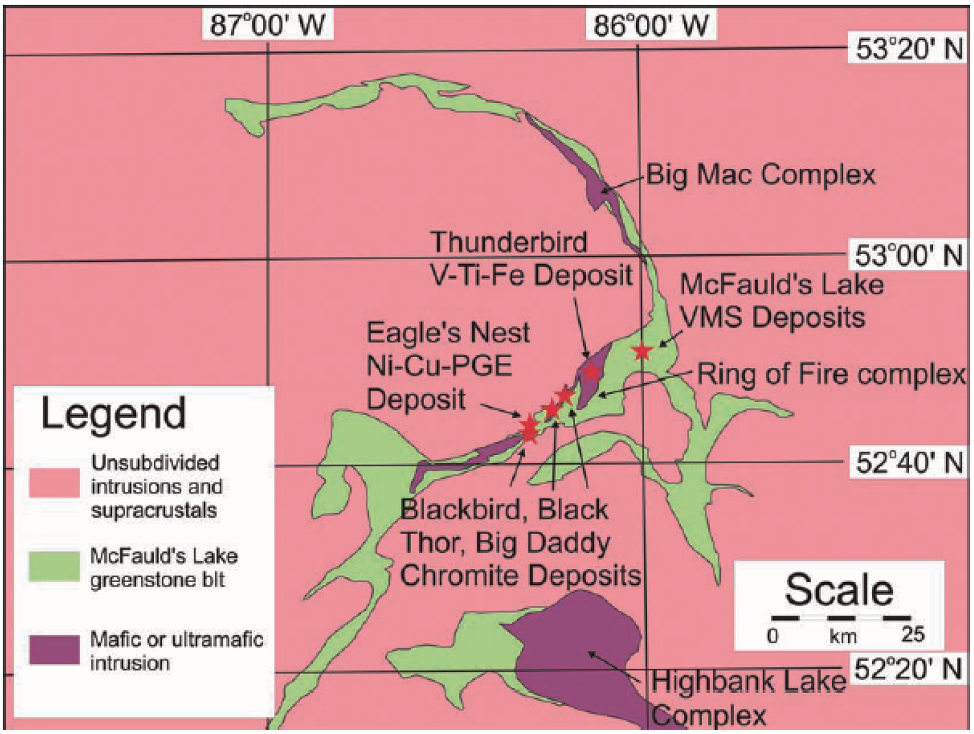

Figure 12. Geological sketch map with known mineralization in the Ring of Fire region. The pink area shows the inferred extent of gneiss domes with Mesoarchean crust formation ages, the green area shows the Neoarchean greenstones and the purple area indicates the Ring of Fire ultramafic-mafic intrusions (Mungall *et al.* 2010).

and $\mathbf{A}$ is a combined matrix of the linear forward operators,

$$\mathbf{A} = \begin{bmatrix} \mathbf{A}^{\mathrm{g}} & \\ & \mathbf{A}^{\mathrm{m}} \end{bmatrix}. \tag{29}$$

As a result of the multinary model transform, the original density and magnetic susceptibility distribution, $\mathbf{m} = [\rho,\ \chi]^T$, have become the transformed distribution, $\widetilde{\mathbf{m}} = [\widetilde{\rho},\ \widetilde{\chi}]^T$. Therefore, the original inverse problem (26) takes the following form:

$$\mathbf{d} = \mathbf{A}[E_{\sigma}^{-1}(\widetilde{\mathbf{m}})] = \widetilde{\mathbf{A}}_{\sigma}(\widetilde{\mathbf{m}}), \tag{30}$$

where $\widetilde{\mathbf{A}}_{\sigma}$ is the new forward modelling operator acting in the transformed model spaces, $\widetilde{\mathbf{m}}$.

Following Zhdanov & Lin (2017), one can demonstrate that the Fréchet derivative $\widetilde{\mathbf{F}}_{\sigma}$ with respect to the new model parameters, $\widetilde{\mathbf{m}}$, can be derived as follows:

$$\widetilde{\mathbf{F}}_{\sigma} = \begin{bmatrix} \mathbf{A}^{\mathrm{g}}\mathbf{g}_{\sigma^{(1)}}^{-1} & \\ & \mathbf{A}^{\mathrm{m}}\mathbf{g}_{\sigma^{(2)}}^{-1} \end{bmatrix}, \tag{31}$$

where $\mathbf{g}_{\sigma^{(j)}}$ is a diagonal matrix formed by the scalar components $g_{\sigma^{(j)}}(m_i^{(j)})$, $i = 1, 2, \ldots N_{\mathrm{m}}, j = 1, 2$; defined above in expressions (24) and (25).

By combining the multinary transformation and the Gramian constraints, we solve the inverse problem (26) based on the minimization of the following Tikhonov parametric functional:

$$\begin{aligned} P_{\sigma}^{\alpha}(\widetilde{\mathbf{m}}^{(1)}, \widetilde{\mathbf{m}}^{(2)}) = &\sum_{j=1}^{2} \left\| \mathbf{W}_{\mathrm{d}^{(j)}}(\widetilde{\mathbf{A}}_{\sigma^{(j)}}(\widetilde{\mathbf{m}}^{(j)}) - \mathbf{d}^{(j)}) \right\|^2 \\ &+ \sum_{j=1}^{2} \alpha^{(j)} \left\| \widetilde{\mathbf{W}}_{\mathrm{m}^{(j)}}(\widetilde{\mathbf{m}}^{(j)} - \widetilde{\mathbf{m}}_{\mathrm{apr}}^{(j)}) \right\|^2 \\ &+ \beta S_{\mathrm{G}}(L\widetilde{\mathbf{m}}^{(1)}, L\widetilde{\mathbf{m}}^{(2)}) \longrightarrow \min. \end{aligned} \tag{32}$$

In the case of joint multinary inversion with structural constraint, one can apply the gradient operator, $L = \nabla$, to enhance the similarities of physical boundaries of anomalous bodies.

We apply the regularized conjugate gradient (RCG) method to find the global minimum of the parametric functional, P_{σ}^{α} (Zhdanov 2002, 2015):

$$\begin{aligned} \mathbf{r}_n &= \widetilde{\mathbf{A}}_{\sigma}(\widetilde{\mathbf{m}}) - \mathbf{d}, \\ \mathbf{l}_n^{\sigma} &= \widetilde{\mathbf{F}}_{\sigma,n}^{T}\mathbf{W}_{\mathrm{d}}^{2}\mathbf{r}_n + \alpha_n \mathbf{W}_{\mathrm{m}}^{2}(\widetilde{\mathbf{m}}_n - \widetilde{\mathbf{m}}_{\mathrm{apr}}) + \beta_n \mathbf{l}_{Gn}^{(j)}, \\ \widetilde{\mathbf{l}}_n^{\sigma} &= \mathbf{l}_n^{\sigma} + \frac{\left\| \mathbf{l}_n^{\sigma} \right\|^2}{\left\| \mathbf{l}_{n-1}^{\sigma} \right\|^2} \widetilde{\mathbf{l}}_{n-1}^{\sigma}, \widetilde{\mathbf{l}}_0^{\sigma} = \mathbf{l}_0^{\sigma}, \\ k_n^{\sigma} &= (\widetilde{\mathbf{l}}_n^{\sigma}, \mathbf{l}_n^{\alpha}) / \left[\left\| \mathbf{W}_{\mathrm{d}} \widetilde{\mathbf{F}}_{\sigma,n} \widetilde{\mathbf{l}}_n^{\sigma} \right\|^2 + \alpha_n \left\| \mathbf{W}_{\mathrm{m}} \widetilde{\mathbf{l}}_n^{\sigma} \right\|^2 + \beta_n \left\| \mathbf{G}_{\mathrm{m}_n} \widetilde{\mathbf{l}}_n^{\alpha} \right\|^2 \right], \\ \widetilde{\mathbf{m}}_{n+1} &= \widetilde{\mathbf{m}}_n - k_n^{\sigma} \widetilde{\mathbf{l}}_n^{\sigma}, \end{aligned} \tag{33}$$

where the steepest ascent directions of the Gramian stabilizing functionals , $\mathbf{l}_{Gn}^{(j)}$, are given in the Appendix. The regularization parameters, α_n and β_n, are usually selected as $\alpha_n = \alpha_1 \cdot q^{n-1}$ and $\beta_n = \beta_1 \cdot q^{n-1}$, where constant q is a small number, $0 < q < 1$. In the following sections, q was set at 0.9, and the initial coefficients, $\alpha_1^{(j)}$ and β_1, are chosen as follows:

$$\alpha_1^{(j)} = \frac{\left\| \mathbf{W}_{\mathrm{d}^{(j)}}(\widetilde{\mathbf{A}}_{\sigma^{(j)}}(\widetilde{\mathbf{m}}_1^{(j)}) - \mathbf{d}^{(j)}) \right\|^2}{\left\| \widetilde{\mathbf{W}}_{\mathrm{m}^{(j)}}(\widetilde{\mathbf{m}}_1^{(j)} - \widetilde{\mathbf{m}}_{\mathrm{apr}}^{(j)}) \right\|^2}, j = 1, 2, \tag{34}$$

$$\beta_1 = \frac{\sum_{j=1}^{2} \left\| \mathbf{W}_{\mathrm{d}^{(j)}}(\widetilde{\mathbf{A}}_{\sigma^{(j)}}(\widetilde{\mathbf{m}}_1^{(j)}) - \mathbf{d}^{(j)}) \right\|^2}{S_{\mathrm{G}}(L\widetilde{\mathbf{m}}_1^{(1)}, L\widetilde{\mathbf{m}}_1^{(2)})}. \tag{35}$$

In some circumstances, we would like to constrain the inverted parameters within the given boundaries, $[\widetilde{m}_{\min}^{(j)}, \widetilde{m}_{\max}^{(j)}]$. For example,

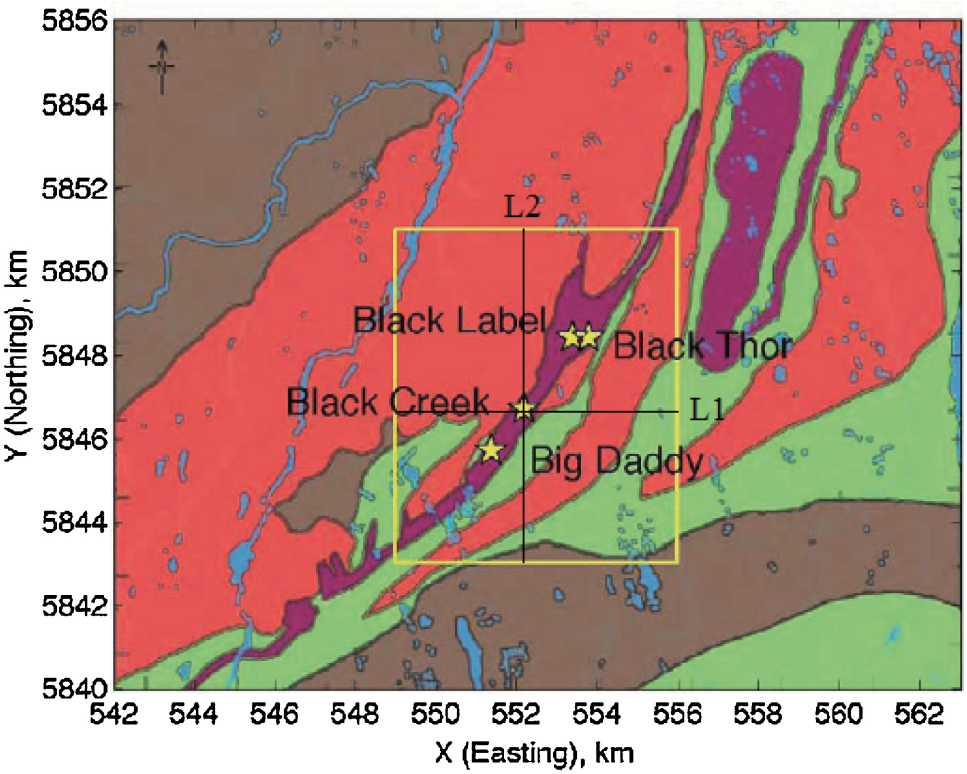

Figure 13. Target area (rectangular box) of the Ring of Fire zone overlapped with regional geological sketch map (adapted from Balch *et al.* 2010; Zhu & Zhdanov 2013).

the magnetic susceptibility obtained from the inversion of TMI data should be non-negative. These constraints can be implemented replacing the transformed parameters, $\widetilde{\mathbf{m}}^{(j)}$, with the new parameters, $\mathbf{x}^{(j)}$:

$$\mathbf{x}^{(j)} = \left[x_1^{(j)}, x_2^{(j)}, \ldots x_{N_\mathrm{m}}^{(j)}\right], \; j = 1, 2; \tag{36}$$

where

$$m_k^{(j)} = \frac{m_{\max}^{(j)} e^{x_k^{(j)}} + m_{\min}^{(j)}}{\mathrm{e}^{x_k^{(j)}} + 1}, \; j = 1, 2; \; k = 1, 2, \ldots, N_\mathrm{m}. \tag{37}$$

As a result, the inversion should be run for the new model parameters, $\mathbf{x}^{(j)}$. In this case, the Gramian term $S_\mathrm{G}(L\widetilde{\mathbf{m}}^{(1)}, L\widetilde{\mathbf{m}}^{(2)})$ has to be modified as follows:

$$S_\mathrm{G}(L\widetilde{\mathbf{m}}^{(1)}, L\widetilde{\mathbf{m}}^{(2)}) = S_\mathrm{G}\left(L\left[\frac{m_{\max}^{(1)}\mathrm{e}^{\mathbf{x}^{(1)}} + m_{\min}^{(1)}}{\mathrm{e}^{\mathbf{x}^{(1)}} + 1}\right], \; L\left[\frac{m_{\max}^{(2)}\mathrm{e}^{\mathbf{x}^{(2)}} + m_{\min}^{(2)}}{\mathrm{e}^{\mathbf{x}^{(2)}} + 1}\right]\right). \tag{38}$$

In order to obtain the physical properties in reasonable ranges, we will apply some reasonable boundaries to the transformed model parameters ($\widetilde{\mathbf{m}}^{(j)}$) in the following sections.

This concludes a description of the method of joint multinary inversion using Gramian constraints.

6 SYNTHETIC MODEL STUDY

In this section, we will test the developed algorithm of joint multinary inversion using 3-D synthetic models with two dipping dikes, which have different sizes, physical properties and burial depths. We will present two model studies for the anomalous targets based on different combinations of densities and magnetic susceptibilities. In this section, we will consider the following four cases for the inversions of gravity and magnetic data:

1) separate minimum norm inversions,

2) joint minimum norm inversion with a structural Gramian constraint ($L = \nabla$),

3) separate multinary inversions, and

4) joint multinary inversion with a structural Gramian constraint ($L = \nabla$).

6.1 Model study 1

In this model study, the depth of the top of left-dipping dike is set as 100 m, while the bottom boundary is at a depth of 300 m; the relatively large right body vertically ranges from 200 to 600 m. The density and magnetic susceptibility of the left dike are 0.2 g cm^{-3} and 0.02 SI, respectively, while the right dike has a density of 0.6 g cm^{-3} and the magnetic susceptibility of 0.06 SI. The values of the background's physical properties were set at 0. The magnetic field was computed for $H_0 = 50\,000$ (total magnetic field), $I = 90^\circ$ (inclination) and $D = 0^\circ$ (declination). We use ternary transformation for this model study in the following cases involving multinary inversion.

Fig. 2 presents a 3-D view of the model. The rectangular contour outlines the location of the cross-section shown in the next figures. We set 100 × 100 measurements on the ground for both gravity and magnetic data, shown as black dots in this figure. Figs 3(a) and (b) show the density and magnetic susceptibility distributions of the corresponding cross-section. The synthetic gravity gradiometry data (G_{zz}, G_{zx} and G_{zy}) and TMI data (T), contaminated by the

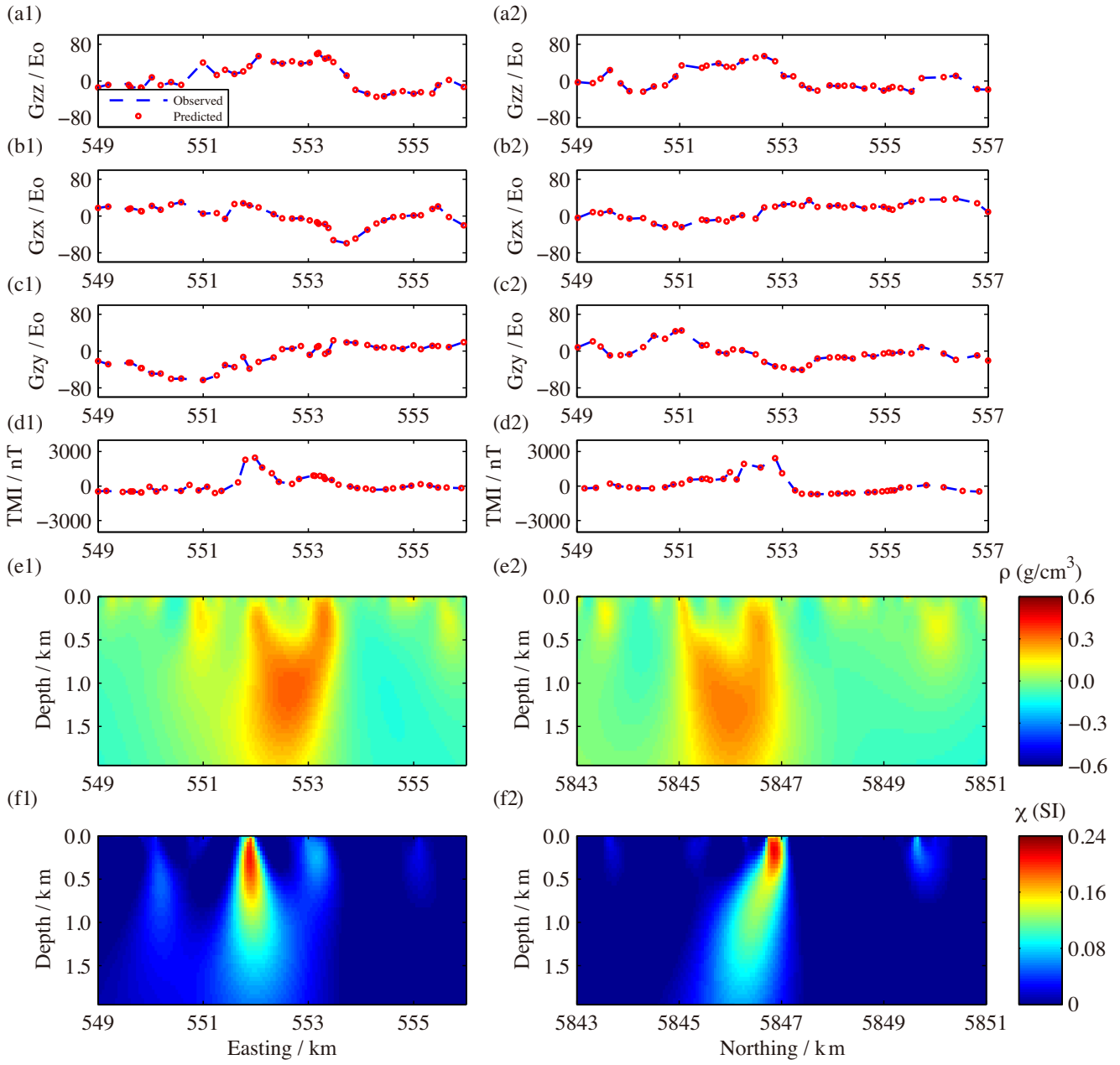

Figure 14. Case 1: panels (a1)–(d1) and (a2)–(d2) show the data fittings for the selected gravity gradiometry components (G_{zz}, G_{zx} and G_{zy}) and the TMI data along the cross-sections, L1 and L2, respectively, while panels (e1)–(f1) and (e2)–(f2) present the corresponding vertical cross-sections of the recovered anomalous density and magnetic susceptibility distributions, respectively. The results were obtained from the separate inversions.

random noise levels of 1 Eo and 5 nT, respectively, were used as the synthetic data.

6.1.1 Case 1: separate minimum norm inversions

In case 1, we applied the minimum norm stabilizing functional for separate inversions of the gravity and magnetic data. The iterative processes for both gravity and magnetic inversions took 37 iterations to reach the misfit level of 4 per cent. Figs 4(a)–(d) show the synthetic data (dashed line) versus the predicted data (dotted line) along the cross-section in Fig. 2 for the full tensor gravity gradiometry (FTG) components, G_{zz}, G_{zx}, G_{zy} and TMI data; while Figs 4(e) and (f) present the cross-sections of the recovered density and magnetic susceptibility distributions, respectively. As we can see, the inversion images present the right dike well, however, the distributions of the physical properties are diffused and unfocused. Meanwhile, the left recovered anomalous body was almost burried in the background.

6.1.2 Case 2: joint minimum norm inversion with structural Gramian constraint

In case 2, we applied the joint inversion algorithm with structural Gramian constraints ($L = \nabla$) to the synthetic gravity and magnetic

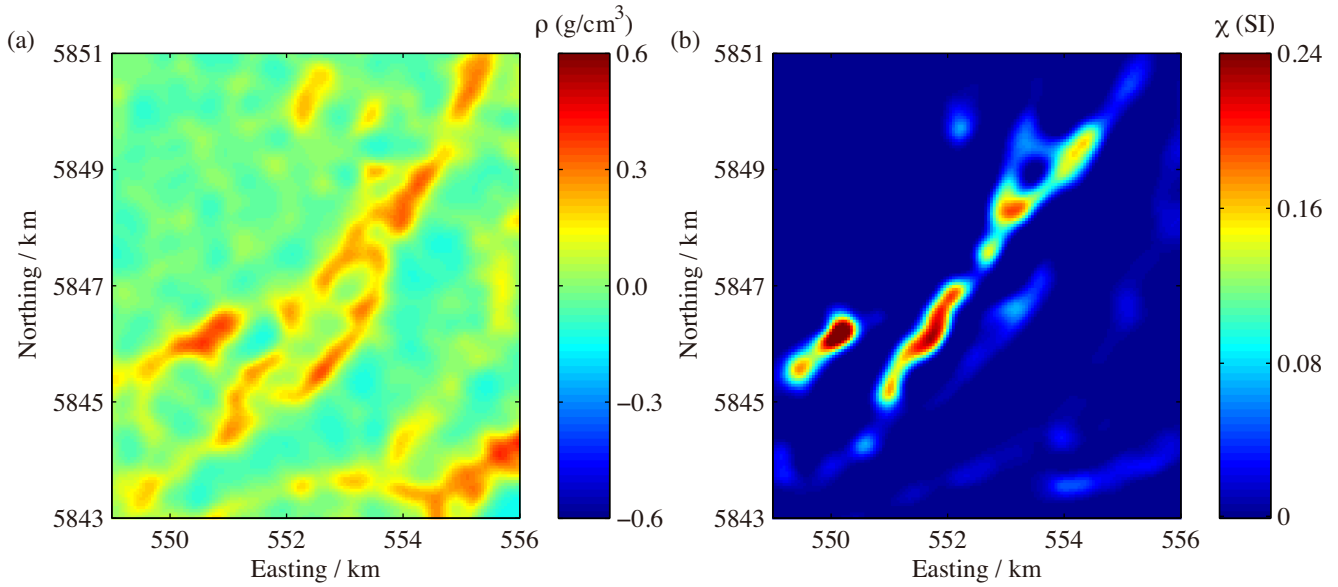

Figure 15. Case 1: horizontal cross-sections of the recovered anomalous density (panel a) and magnetic susceptibility (panel b) distributions corresponding to the depth of 350 m, generated by the separate inversions.

data. The inversion process converged until the misfit reached the level of 4 per cent at the iteration number, 65. Figs 5(a)–(d) provide the data fittings, while Figs 5(e) and (f) show the vertical sections of the inverse density and magnetic susceptibility models, respectively. We can see that, after applying the Gramian constraints, the recovered distributions of the physical properties became slightly compact, however, the resolution of the anomalous bodies is still low.

6.1.3 Case 3: separate multinary inversions

In this test, we applied separate inversions with ternary transformation. The ternary functions were set to recover three discrete densities of 0, 0.2 and 0.6 g cm^{-3}, and three discrete magnetic susceptibilities of 0, 0.02 and 0.06 SI (where value 0 represents the background model) with fixed standard deviations of $\sigma^{(1)} = 0.06$ and $\sigma^{(2)} = 0.006$, respectively. The representations of the ternary model transforms for density (ρ) and magnetic susceptibility (χ) and their derivatives are shown in Fig. 6. In order to keep the recovered physical properties within a reasonable range, we implemented some boundaries to the model parameters, as shown in Fig. 6. The solid lines indicate the actual multinary functions and their derivatives applied to the separate inversions. In such case, the derived physical properties would be always non-negative but not larger than the third discrete values (0.6 and 0.06). The iterative processes of the RCG algorithm were terminated when the misfit reached the level of noise, 4 per cent. Figs 7(a)–(d) indicate same data fittings as the previous cases, and Figs 7(e) and (f) show the vertical cross-sections of the recovered density and magnetic susceptibility distributions, respectively. It is obvious that the spatial boundaries of the anomalous bodies recovered from the gravity and magnetic data are not consistent with each other. The multinary inversion of gravity data reconstructed the two anomalous bodies very well, however, the magnetic inversion recovered only the right body with sharp boundaries.

6.1.4 Case 4: joint multinary inversion with structural Gramian constraints

In the final case, we analysed the joint multinary inversion with structural Gramian constraints. We used the same ternary transformations as in case 3. The joint inversion reached the misfit level of 4 per cent at the iteration number, 60, which shows a faster convergence than in the case of separate multinary inversions. Figs 12(a)–(d) provide data fittings for the selected gravity gradiometry data (G_{zz}, G_{zx} and G_{zy}) and TMI data, while Figs 12(e) and (f) present the vertical sections of the inverse models for the density and magnetic susceptibility distributions, respectively. We can find the consistent boundaries of the anomalous bodies in both inverse models, as well as the similar geological trends of the two anomalous bodies in comparison to the synthetic models in Fig. 3. These results demonstrate that the joint multinary inversion not only makes it possible to improve the resolution of the inverse images, but also recovers the anomalous bodies at their physical properties, approximate shapes and locations.

6.2 Model study 2

In model study 2, we applied the same 3-D model except the left dike is not magnetic. The goal of this study was to investigate if coincident features in the two solutions can be fabricated by the Gramian method. Figs 9(a) and (b) show the density and magnetic susceptibility distributions within the cross-section in Fig. 2. Again, the synthetic gravity gradiometry data (G_{zz}, G_{zx} and G_{zy}) and TMI data (T) were computed by contaminating the random noise levels of 1 Eo and 5 nT, respectively. We will compare the inversion results between separate multinary inversions and joint multinary inversion with structural Gramian constraint. To keep the transformed physical properties having the consistent boundaries in the multinary model space, we applied the same ternary functions and their derivatives as in the previous model study even though there were only two discrete magnetic susceptibilities.

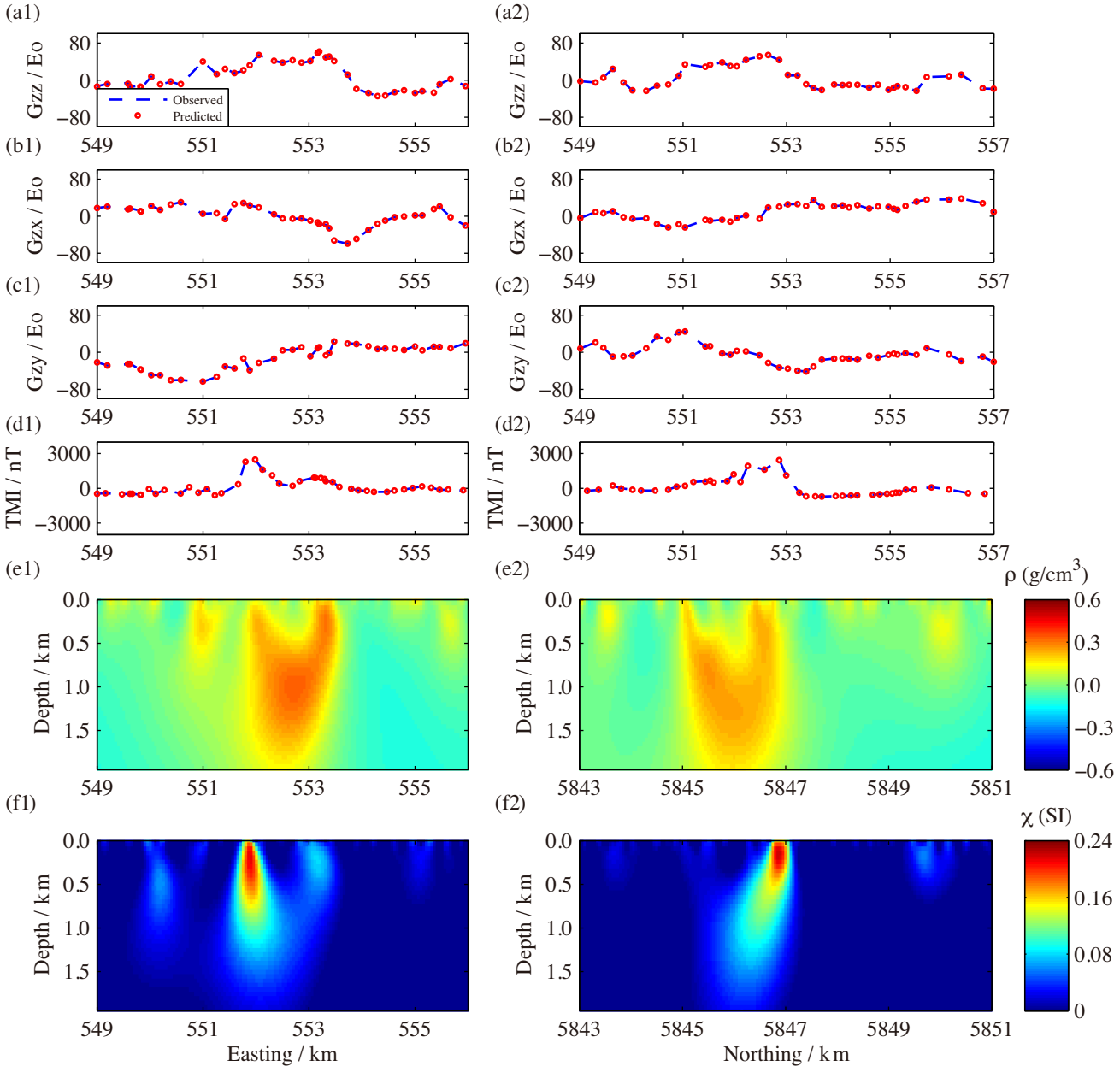

Figure 16. Case 1: panels (a1)–(d1) and (a2)–(d2) show the data fittings for the selected gravity gradiometry components (G_{zz}, G_{zx} and G_{zy}) and the TMI data along the cross-sections, L1 and L2, respectively, while panels (e1)–(f1) and (e2)–(f2) present the corresponding vertical cross-sections of the recovered anomalous density and magnetic susceptibility distributions, respectively. The results were obtained from the joint inversion without multinary transformation.

6.2.1 Case 1: separate multinary inversions

In case 1, we applied the separate inversions with ternary transformation. The iterative processes for both gravity and magnetic inversions were terminated at the misfit level of 4 per cent. Fig. 10 shows the data fittings (panels a–d) and the cross-sections of the recovered density and magnetic susceptibility distributions (panels e–f). As we can see, the distributions of the recovered physical properties are similar to those in case 3 of the previous model study, except the left anomalous body was not shown in Fig. 10(f). This is reasonable because the left dike in the synthetic model was set to be non-magnetic. Next, we will apply the joint multinary inversion algorithm to see how the developed approach can improve the inversion results.

6.2.2 Case 2: joint multinary inversion with structural Gramian constraint

In the final case, we applied structural Gramian constraints to the joint multinary inversion. The joint inversion reached the misfit level of 4 per cent at iteration number, 64. Figs 11(e) and (f) present vertical sections of the inverse models for the density and magnetic

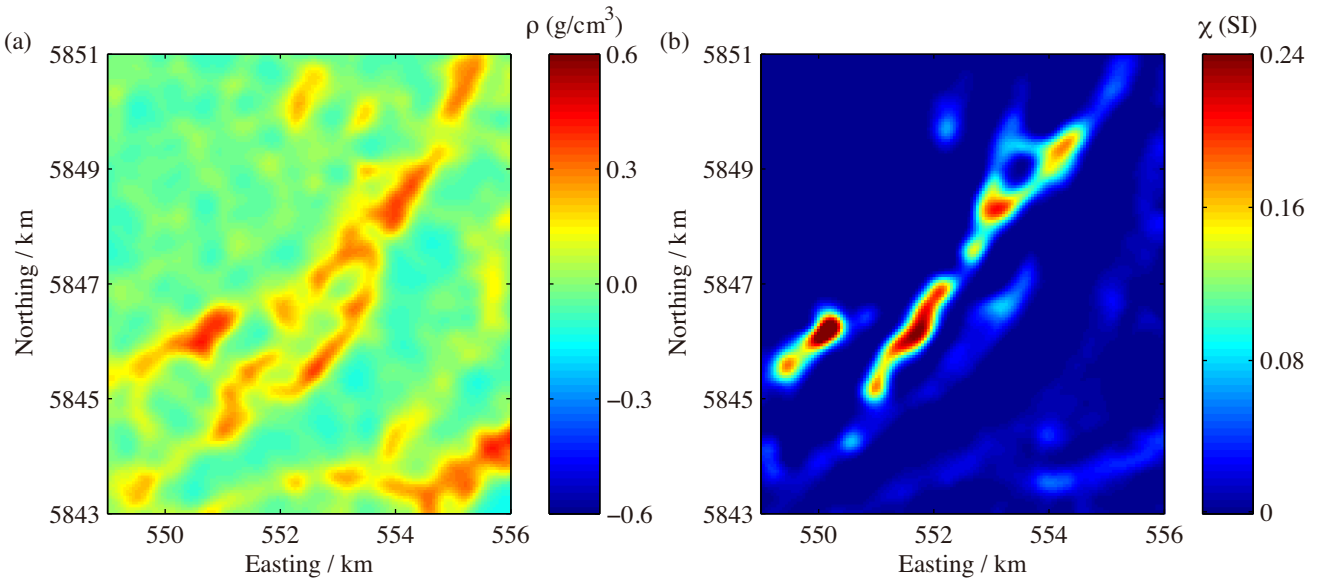

Figure 17. Case 1: horizontal cross-sections of the recovered anomalous density (panel a) and magnetic susceptibility (panel b) distributions corresponding to the depth of 350 m, generated by the joint inversion without multinary transformation.

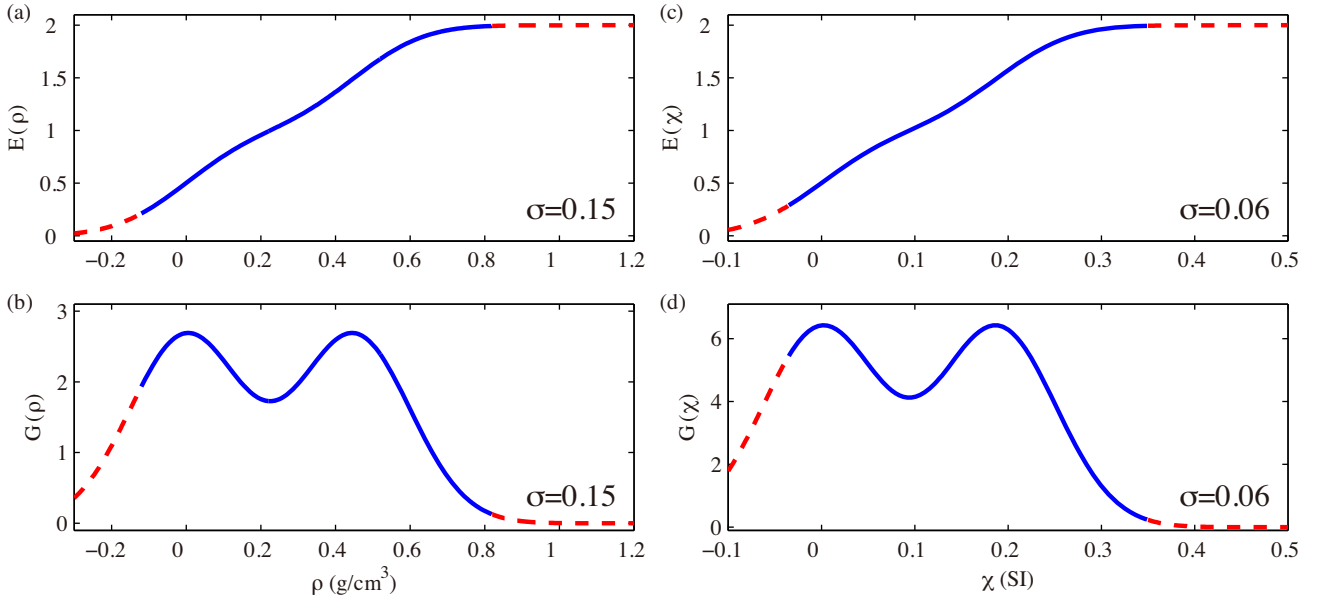

Figure 18. Case 2: panels (a) and (c) show the approximate representations of the binary model transforms for density (ρ) and magnetic susceptibility (χ), respectively, and panels (b) and (d) show their derivatives. The values of the discrete densities and magnetic susceptibilities are as follows: 0 and 0.45 g cm^{-3}, 0 and 0.2 SI; and $\sigma^{(1)} = 0.15$ and $\sigma^{(2)} = 0.06$. The dashed lines in these plots correspond to the values of density and magnetic susceptibility outside of the upper and lower bounds imposed in the inversion.

susceptibility distributions, respectively. While the boundaries of the right anomalous body in both inverse models were consistent, the left body was shown only in the recovered density distribution but almost disappeared in Fig. 11(f). In other words, there was no false structure generated in the cross-section of the inverse magnetic susceptibility model. Thus, the results of model study 2 demonstrate that the Gramian constraints do not require a uniform linear relationship between the parameters or their attributes within the entire model domain. The Gramian constraints can be also applied to the case when multiple relationships between the parameters exist.

7 CASE STUDY: JOINT INVERSION OF GRAVITY AND MAGNETIC DATA IN THE AREA OF MCFAULDS LAKE, ONTARIO

7.1 Regional geology in McFaulds Lake area

McFaulds Lake is located in northwestern Ontario approximately 50 km east of Webequie, where the Eagle's Nest nickel, copper and platinum group element (Ni-Cu-PGE) deposit was discovered. This area is part of a mantle-derived, highly magnetic ultramafic intrusion

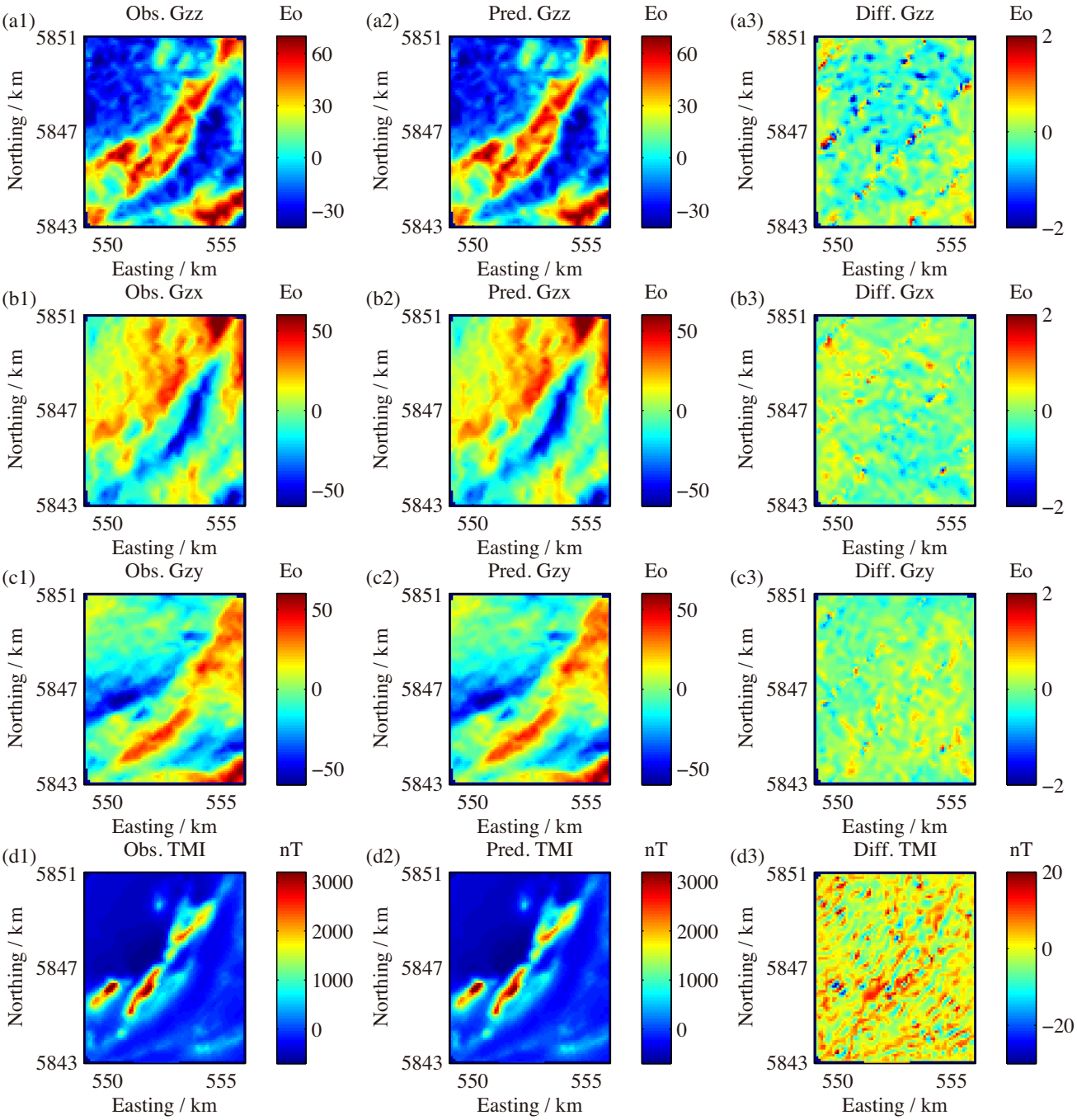

Figure 19. Case 2: maps of the observed and predicted data obtained from the joint inversion with multinary transformation. Panels (a1)–(d1) show the maps of observed gravity components, G_{zx}, G_{zy}, G_{zz} and the TMI component, panels (a2)–(d2) show the corresponding maps of the predicted data and panels (a3)–(d3) show the maps of the differences between the observed and predicted data.

known as the 'Ring of Fire' that has been emplaced along the margin of a major granodiorite pluton within rocks of the Sachigo greenstone belt (Balch *et al.* 2010). Fig. 12 shows a geological sketch map with known mineralization in the Ring of Fire region (Mungall *et al.* 2010). Several economic mineral deposits have been explored in this area, including: magmatic Ni-Cu-PGE, magmatic chromite mineralization, volcanic massive sulfide mineralization and diamonds hosted by kimberlite. The Ring of Fire is composed of mafic metavolcanic flows, felsic metavolcanic flows and pyroclastic rocks and a suite of layered mafic to ultramafic intrusions that trend subparallel with and obliquely cut the westernmost part of the belt, close to a large granitoid batholith lying west of the belt. The major layered intrusion at its base, hosts Ni-Cu-PGE deposits of exceptional grade as well as overlying stratiform chromite deposits further east and higher in the layered intrusion stratigraphy (Ontario Geological Survey and Geological Survey of Canada, 2011; Zhu and Zhdanov, 2013).

Chromite deposits usually occur in layered ultramafic intrusive rocks, which is commonly associated with magnetite and serpentine. Thus one can trace chromite magnetically through its possible

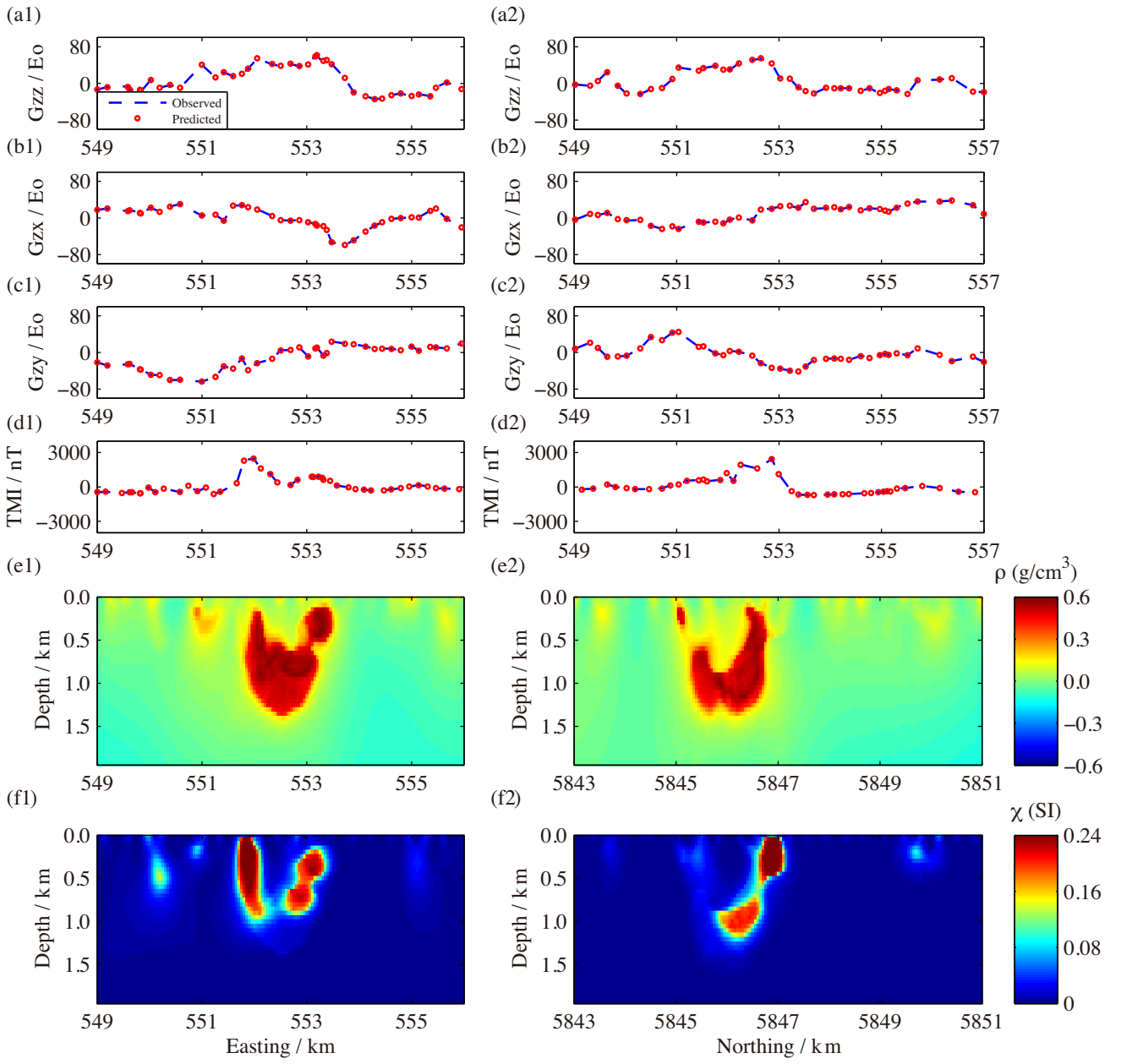

Figure 20. Case 2: panels (a1)–(d1) and (a2)–(d2) show the data fittings for the selected gravity gradiometry components (G_{zz}, G_{zx} and G_{zy}) and the TMI data along the cross-sections, L1 and L2, respectively, while panels (e1)–(f1) and (e2)–(f2) present the corresponding vertical cross-sections of the recovered anomalous density and magnetic susceptibility distributions, respectively. The results were obtained from the joint inversion with multinary transformation.

host rock. On the other hand, since the density of chromitite ranges from 3.6 to 4.0 g cm^{-3}, chromite can be also found in the areas which have large positive gravity anomalies. Accordingly, the airborne geophysical surveys were conducted in the area of McFaulds Lake in 2010, where the airborne gravity gradiometer (AGG) and magnetic data were collected (Ontario Geological Survey and Geological Survey of Canada, 2011). For the preliminary study, we selected a subset of the AGG and magnetic data covering the known chromite mineralization, as shown in Fig. 13 (adapted from Balch *et al.* 2010; Zhu and Zhdanov, 2013). In the target area, there are four chromite deposits: Big Daddy, Black Creek, Black Thor and Black Label. In the following section, we will apply the gravity inversion and magnetic inversion jointly with and without multinary transformation. We will show the cross-sections of two selected lines, L1 and L2 in Fig. 13, which vertically cross the Black Creek.

7.2 Case 1: joint inversion of gravity and magnetic data without multinary transformation

The size of the target area (rectangular box in Fig. 13) was set to be 7 km × 8 km × 2 km and the domain was discretized by prismatic cells of 50 m × 50 m × 50 m. The gravity and gravity gradiometry components, G_{zz}, G_{zx} and G_{zy}, as well as the TMI data were selected for the inversions. The numbers of measurements

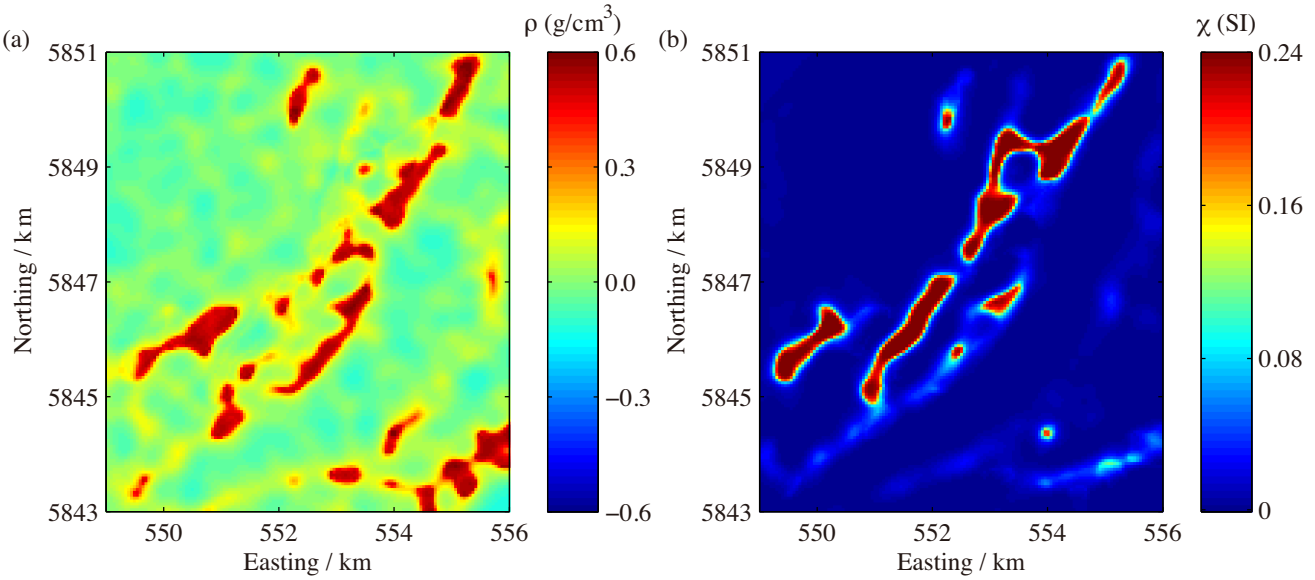

Figure 21. Case 2: horizontal cross-sections of the recovered anomalous density (panel a) and magnetic susceptibility (panel b) distributions corresponding to the depth of 350 m, generated by the joint inversion with multinary transformation.

for the gravity and magnetic surveys in the domain are 963 and 1197, respectively. The stopping criterion of normalized misfit is set as 2 per cent. First we ran the gravity and magnetic inversions separately using the minimum norm stabilizer. The left and right columns of Fig. 14 show the data fittings for the selected data sets and the vertical cross-sections of the predicted density and magnetic susceptibility distributions along the lines, L1 and L2, respectively. Fig. 15 shows the horizontal cross-sections of the recovered density and susceptibility models at a depth of 350 m. All the cross-sections can only provide limited resolution of the geological targets.

Next, we applied the joint inversion of gravity and magnetic data without multinary transformation ($L = \nabla$). Fig. 16 shows the data fittings and the vertical cross-sections of the recovered anomalous density and magnetic susceptibility distributions, respectively. Compared to the previous results, the predicted anomalous targets become slightly compact, but overall the targets are still diffused. The horizontal anomalous density and magnetic susceptibility slices are shown in Fig. 17. For the mineral exploration, one may expect a more compact predicted mineral body with sharp boundary. In order to provide a more convincing geological model, we applied the joint inversion with multinary transformation.

7.3 Case 2: joint inversion of gravity and magnetic data with multinary transformation

In this section, we applied the joint inversion algorithm with multinary transformation and structural Gramian constraint ($L = \nabla$). Based on the known geological information (e.g. borehole data), the multinary functions were set to recover two discrete densities of 0 and 0.45 g cm^{-3}, and two discrete magnetic susceptibilities of 0 and 0.2 SI (where value 0 represents the background model) with fixed standard deviations of $\sigma^{(1)} = 0.15$ and $\sigma^{(2)} = 0.06$, respectively. The representations of the multinary model transforms for anomalous density (ρ) and magnetic susceptibility (χ) and their derivatives are shown in Fig. 18. The solid lines indicate the valid ranges of the binary functions and their derivatives applied to the inversions. The stopping criterion of the normalized misfit is also set as 2 per cent.

Fig. 19 shows a comparison between the observed (panels a1–d1) and predicted data (panels a2–d2) representing the files of the selected gravity gradiometry components (G_{zz}, G_{zx} and G_{zy}) and the magnetic field (TMI). In this figure, we observe a good data fitting, which is illustrated by the maps of the differences between the observed and predicted data through Figs 19(a3)–(d3). Figs 20(e1)–(f1) and (e2)–(f2) show the vertical cross-sections of the recovered anomalous density and magnetic susceptibility distributions corresponding to lines, L1 and L2 in Fig. 13, respectively. For the L1 cross-section, the upper boundaries of the recovered mineral body can be clearly seen from the joint inversion results, while the lower part of the body is less magnetic but much denser. For the L2 cross-section, the gravity inversion result shows two vertically intrusive dikes with higher anomalous densities, meanwhile the magnetic inversion provides that the dike on the right contains more magnetic minerals, which might correspond to the chromite mineralization in the area of Black Creek. Fig. 21 shows the horizontal anomalous density and magnetic susceptibility slices associated with the depth of 350 m. All the cross-sections and slices illustrate the anomalous targets with sharp and partially consistent boundaries, which provides more details about the mineralizations compared to the previous case.

8 CONCLUSION

We have developed a method of joint inversion of multimodal geophysics data based on the multinary transform and Gramian constraints. This method was applied to the problem of the joint inversion of potential fields. We have demonstrated that this inverse problem can be solved using a gradient-type optimization method. We have tested this method with 3-D synthetic models using ternary model transformation, which demonstrated that the joint multinary inversion can recover the approximate sizes, locations and the physical properties of the anomalous bodies well. We have also applied this method in the joint inversion of gravity and magnetic data of the McFaulds Lake area in northwestern

Ontario, Canada, and the joint inversion results provide a reasonable geological model for the exploration of magmatic chromite deposits.

ACKNOWLEDGEMENTS

The authors acknowledge support from the University of Utah's Consortium for Electromagnetic Modeling and Inversion (CEMI) and TechnoImaging. We also thank the Ontario Geological Survey and Geological Survey of Canada for providing the airborne geophysical data.

We thank Dr Ed Biegert and Dr Mark Pilkington for their valuable suggestions and comments which helped to improve the manuscript.

REFERENCES

Abubakar, A., Gao, G., Havashy, T. M. & Liu, J., 2012. Joint inversion approaches for geophysical electromagnetic and elastic full-waveform data, *Inverse Probl.,* **28**(5), doi:10.1088/0266-5611/28/5/055016.

Balch, S.J., Mungall, J.E. & Niemi, J.E., 2010. Present and future geophysical methods for Ni-Cu-PGE exploration: lessons from McFaulds Lake, northern Ontario, in *The Challenge of Finding New Mineral Resources: Global Metallogeny, Innovative Exploration, and New Discoveries,* pp. 559–572 , eds Goldfarb, R.J., Marsh, E.E. & Monecke, T., Society of Economic Geologists.

Bosch, M., Guillen, A. & Ledru, P., 2001. Lithologic tomography: an application to geophysical data from the Cadomian belt of northern Brittany, France, *Tectonophysics,* **331**(1–2), 197–227.

Colombo, D. & De Stefano, M., 2007. Geophysical modeling via simultaneous joint inversion of seismic, gravity, and electromagnetic data: application to prestack depth imaging, *Leading Edge,* **26**(3), 326–331.

Dorn, O. & Lesselier, D., 2006. Level set methods for inverse scattering, *Inverse Probl.,* **22**(4), doi:10.1088/0266-5611/22/4/R01.

Gallardo, L.A. & Meju, M.A., 2003. Characterization of heterogeneous near-surface materials by joint 2D inversion of DC resistivity and seismic data, *Geophys. Res. Lett.,* **30**(13), doi:10.1029/2003GL017370.

Gallardo, L.A. & Meju, M.A., 2004. Joint two-dimensional DC resistivity and seismic travel time inversion with cross-gradients constraints, *J. geophys. Res.,* **109**(B3), doi:10.1029/2003JB002716.

Gallardo, L.A. & Meju, M.A., 2011. Structure-coupled multiphysics imaging in geophysical sciences, *Rev. Geophys.,* **49**(1), doi:10.1029/2010RG000330.

Gao, G., Abubakar, A. & Habashy, T.M., 2012. Joint petrophysical inversion of electromagnetic and full-waveform seismic data, *Geophysics,* **77**(3), WA3–WA18.

Haber, E. & Oldenburg, D., 1997. Joint inversion: a structural approach, *Inverse Probl.,* **13**(1), 63–77.

Krahenbuhl, R.A. & Li, Y., 2006. Inversion of gravity data using a binary formulation, *Geophys. J. Int.,* **167**(2), 543–556.

Lin, W. & Zhdanov, M.S., 2017. Joint inversion of seismic and gravity gradiometry data using Gramian constraints, in *2017 SEG International Exposition and Annual Meeting,* pp. 1734–1738, Houston, TX.

Mungall, J.E., Harvey, J.D., Balch, S.J., Azar, B., Atkinson, J. & Hamilton, M.A., 2010. Eagle's nest: a magmatic Ni-sulfide deposit in the James Bay Lowlands, Ontario, Canada, in *The Challenge of Finding New Mineral Resources: Global Metallogeny, Innovative Exploration, and New Discoveries,* pp. 539–557 , eds Goldfarb, R.J., Marsh, E.E. & Monecke, T., Society of Economic Geologists.

Ontario Geological Survey and Geological Survey of Canada, 2011. Ontario airborne geophysical surveys, gravity gradiometer and magnetic data, grid and profile data (ASCII and Geosoft® formats) and vector data, McFaulds Lake area, Ontario Geological Survey, Geophysical Data Set 1068.

Osher, S. & Sethian, J.A., 1988. Fronts propagating with curvature-dependent speed: algorithms based on Hamilton-Jacobi formulations, *J. Comput. Phys.,* **79**(1), 12–49.

Portniaguine, O. & Zhdanov, M.S., 1999. Focusing geophysical inversion images, *Geophysics,* **64**(3), 874–887.

Santosa, F., 1996. A level set approach for inverse problems involving obstacles, *ESAIM: Control Optimisation and Calculus of Variations,* **1,** 17–33.

Vozoff, K. & Jupp, D.L.B., 1975. Joint inversion of geophysical data, *Geophys. J. Int.,* **42**(3), 977–991.

Zhdanov, M.S., 2002. *Geophysical Inverse Theory and Regularization Problems,* Elsevier.

Zhdanov, M.S., 2009. New advances in regularized inversion of gravity and electromagnetic data, *Geophys. Prospect.,* **57**(4), 463–478.

Zhdanov, M.S., 2015. *Inverse Theory and Applications in Geophysics,* Elsevier.

Zhdanov, M.S. & Cox, L., 2013. Multinary inversion of geophysical data, in *Proceedings of the Annual Meeting of the Consortium for Electromagnetic Modeling and Inversion,* pp. 125–136, Salt Lake City, UT.

Zhdanov, M.S. & Lin, W., 2017. Adaptive multinary inversion of gravity and gravity gradiometry data, *Geophysics,* **82**(6), G101–G114.

Zhdanov, M.S., Gribenko, A. & Wilson, G., 2012. Generalized joint inversion of multimodal geophysical data using Gramian constraints, *Geophys. Res. Lett.,* **39**(9), doi:10.1029/2012GL051233.

Zheglova, P. & Farquharson, C., 2018. Multiple level-set joint inversion of traveltime and gravity data with application to ore delineation: a synthetic study, *Geophysics,* **83**(1), R13–R30.

Zhu, Y., 2017. Joint inversion of potential field and electromagnetic data using Gramian constraints, *PhD thesis,* The University of Utah, p. 107.

Zhu, Y., Zhdanov, M.S. & Čuma, M., 2013. Gramian constraints in the joint inversion of airborne gravity gradiometry and magnetic data, in *Proceedings of the Annual Meeting of the Consortium for Electromagnetic Modeling and Inversion,* pp. 1166–1170, Salt Lake City, UT.

APPENDIX: STEEPEST ASCENT DIRECTIONS OF THE GRAMIAN STABILIZING FUNCTIONAL

A stabilizing functional formed by the Gramian of the transformed model parameters can be expressed, using matrix notations, as follows:

$$S_{\mathrm{G}}(L\mathbf{m}^{(1)}, L\mathbf{m}^{(2)}) = S_{\mathrm{G}}(\tilde{\mathbf{m}}^{(1)}, \tilde{\mathbf{m}}^{(2)})$$

$$= \left[\left(\tilde{\mathbf{m}}^{(1)}\right)^t \left(\tilde{\mathbf{m}}^{(1)}\right)\right]\left[\left(\tilde{\mathbf{m}}^{(2)}\right)^t \left(\tilde{\mathbf{m}}^{(2)}\right)\right] - \left[\left(\tilde{\mathbf{m}}^{(1)}\right)^t \left(\tilde{\mathbf{m}}^{(2)}\right)\right]^2, \qquad \text{(A1)}$$

where L is a linear operator that determines the type of the constraints imposed by the Gramian stabilizer; $\tilde{\mathbf{m}}^{(1)}$ and $\tilde{\mathbf{m}}^{(2)}$ are the vectors of the transformed model parameters within the inversion domain, respectively, and upper script 't' denotes transposition.

Let us calculate the first variation:

$$\delta S_{\mathrm{G}}(\tilde{\mathbf{m}}^{(1)}, \tilde{\mathbf{m}}^{(2)}) = \delta_{\mathbf{m}^{(1)}} S_{\mathrm{G}}(\tilde{\mathbf{m}}^{(1)}, \tilde{\mathbf{m}}^{(2)}) + \delta_{\mathbf{m}^{(2)}} S_{\mathrm{G}}(\tilde{\mathbf{m}}^{(1)}, \tilde{\mathbf{m}}^{(2)}). \qquad \text{(A2)}$$

The first variations of the Gramian stabilizer, $\delta_{\mathbf{m}^{(1)}} S_{\mathrm{G}}$ and $\delta_{\mathbf{m}^{(2)}} S_{\mathrm{G}}$ can be calculated as follows:

$$\delta_{\mathbf{m}^{(1)}} S_{\mathrm{G}}(\tilde{\mathbf{m}}^{(1)}, \tilde{\mathbf{m}}^{(2)}) = 2\left[\left(\delta\tilde{\mathbf{m}}^{(1)}\right)^t \left(\tilde{\mathbf{m}}^{(1)}\right)\right]\left[\left(\tilde{\mathbf{m}}^{(2)}\right)^t \left(\tilde{\mathbf{m}}^{(2)}\right)\right] - 2\left[\left(\delta\tilde{\mathbf{m}}^{(1)}\right)^t \left(\tilde{\mathbf{m}}^{(2)}\right)\right]\left[\left(\tilde{\mathbf{m}}^{(1)}\right)^t \left(\tilde{\mathbf{m}}^{(2)}\right)\right], \qquad \text{(A3)}$$

$$\delta_{\mathbf{m}^{(2)}} S_{\mathrm{G}}(\widetilde{\mathbf{m}}^{(1)},\widetilde{\mathbf{m}}^{(2)}) = 2\left[\left(\widetilde{\mathbf{m}}^{(1)}\right)^t\left(\widetilde{\mathbf{m}}^{(1)}\right)\right]\left[\left(\delta\widetilde{\mathbf{m}}^{(2)}\right)^t\left(\widetilde{\mathbf{m}}^{(2)}\right)\right] - 2\left[\left(\delta\widetilde{\mathbf{m}}^{(2)}\right)^t\left(\widetilde{\mathbf{m}}^{(1)}\right)\right]\left[\left(\widetilde{\mathbf{m}}^{(1)}\right)^t\left(\widetilde{\mathbf{m}}^{(2)}\right)\right]. \quad \text{(A4)}$$

Taking $\left(\delta\mathbf{m}^{(1)}\right)^t$ out of the brackets in eq. (A3), we arrive at the following formula:

$$\delta_{\mathbf{m}^{(1)}} S_{\mathrm{G}}(\widetilde{\mathbf{m}}^{(1)},\widetilde{\mathbf{m}}^{(2)}) = 2\left(\delta\widetilde{\mathbf{m}}^{(1)}\right)^t \mathbf{l}_{\mathrm{G}}^{(1)},$$

where the steepest ascent direction, $\mathbf{l}_{\mathrm{G}}^{(1)}$, is given by the following expression:

$$\mathbf{l}_{\mathrm{G}}^{(1)} = \left(\widetilde{\mathbf{m}}^{(1)}\right)\left[\left(\widetilde{\mathbf{m}}^{(2)}\right)^t\left(\widetilde{\mathbf{m}}^{(2)}\right)\right] - \left(\widetilde{\mathbf{m}}^{(2)}\right)\left[\left(\widetilde{\mathbf{m}}^{(1)}\right)^t\left(\widetilde{\mathbf{m}}^{(2)}\right)\right]. \quad \text{(A5)}$$

Similarly, we can find

$$\mathbf{l}_{\mathrm{G}}^{(2)} = \left(\widetilde{\mathbf{m}}^{(2)}\right)\left[\left(\widetilde{\mathbf{m}}^{(1)}\right)^t\left(\widetilde{\mathbf{m}}^{(1)}\right)\right] - \left(\widetilde{\mathbf{m}}^{(1)}\right)\left[\left(\widetilde{\mathbf{m}}^{(1)}\right)^t\left(\widetilde{\mathbf{m}}^{(2)}\right)\right]. \quad \text{(A6)}$$